REVISION 2

Zirconolite from Larvik Plutonic Complex, Norway, its relationship to stefanweissite and nöggerathite, and contribution to the improvement of zirconolite endmember systematics

Jakub Haifler[1,*], Radek Škoda[1], Jan Filip[2], Alf Olav Larsen[3], Jan Rohlíček[4]

[1] Department of Geological Sciences, Masaryk University, Kotlářská 2, 611 37 Brno, Czech Republic; [*]E-mail: haifler.j@sci.muni.cz

[2] Regional Centre of Advanced Technologies and Materials, Palacký University Olomouc, Šlechtitelů 27, 783 71 Olomouc, Czech Republic

[3] Bamseveien 5, N-3960 Stathelle, Norway

[4] Institute of Physics of the Czech Academy of Sciences, Na Slovance 2, 182 21 Prague 8, Czech Republic

ABSTRACT

The very first description of zirconolite, originally called *polymignyte*, discovered in alkaline pegmatites within the Larvik Plutonic Complex (LPC), Norway, was published almost 200 years ago. We studied zirconolite from 3 occurrences located in this region using modern instrumental techniques – X-ray powder diffraction (XRPD) upon thermal annealing of initially radiation-damaged mineral, electron probe microanalysis and Mössbauer spectroscopy. The initial XRPD pattern lacked any sharp diffraction maxima, as the accumulated radiation dose exceeded a critical value of c. 10^{16} α-decays/mg. Annealing at 400–800 °C induced recrystallisation to a transitional, cubic phase interpreted to have a disordered, defect fluorite structure (space group *Fm-3m*; unit cell parameters [Å]: a = 5.1047(4), V = 133.02(2) Å^3), with XRPD pattern very similar to that of a cubic ZrO_2. The powder diffraction pattern obtained after a phase transition at 900 °C and refined using Rietveld method shows participation of *-3O* (wt. fraction of c. 60%,

space group *Cmca*, unit cell parameters [Å]: a = 7.2664(8), b = 14.1877(15), c = 10.1472(12), V = 1046.1(2) Å^3) and -*3T* (wt. fraction of c. 40%, space group $P3_121$, unit cell parameters [Å]: a = 7.2766(6), c = 17.0627(15), V = 752.42(11) Å^3) zirconolite polytypes. However, the crystal habits of zirconolite from the LPC show a distinct orthorhombic symmetry. Although the chemical compositions of the grains are far from ideal zirconolite and a large number of elements are involved in high concentrations (up to c. 17 wt% REE_2O_3, ≤7 wt% $ACTO_2$, ≤18 wt% $Me^{5+}{}_2O_5$, ≤9 wt% $Me^{2+}O + Me^{3+}{}_2O_3$, $Fe^{3+}/(Fe^{3+}+Fe^{2+}) \approx 0.2$, where ACT = Th + U, Me^{5+} = Nb ± Ta, Me^{2+} = Fe^{2+} ± Mg, $Me^{3+} \approx Fe^{3+}$), the compositional variability is relatively limited. To quantitatively and clearly describe the two distinct compositional trends observed, we introduced a concept called "*edgemembers*", so that mixing is approximated to occur between two terminal compositions situated at two edges of the zirconolite composition space. These marginal compositions were determined from observed compositional trends, i.e. heterovalent substitution of Me^{5+} for Ti in octahedral sites and ACT-enrichment associated with increasing Ti/Me^{5+} ratio. This approach provides general substitution vectors for both, Håkestad-type mode (ACT + 3 Ti + Me^{3+} = Ca + 3 Me^{5+} + Me^{2+}), and for Stålaker-type mode (0.7 ACT + 0.5 REE + 0.9 Ti + 0.7 Me^{3+} + 0.05 Zr = 1.2 Ca + 1.3 Me^{5+} + 0.3 Me^{2+} + 0.05 Mn), respectively. In terms of chemical composition, the studied zirconolite corresponds to recently approved zirconolite-related minerals stefanweissite (for Ca>REE) and nöggerathite (for REE>Ca). Based on a careful analysis of zirconolite composition space, we show that our observed Håkestad-type compositional trend, as well as high number of published zirconolite compositions worldwide (with $Me^{2+} + Me^{3+}$ sum of c. 1 atom per 14 O), are well approximated by a modified endmember set comprising $Ca_2Zr_2Me^{5+}{}_2TiMe^{2+}O_{14}$ – $REE_2Zr_2Ti_3Me^{2+}O_{14}$ – $CaACTZr_2Ti_3Me^{2+}O_{14}$ – $CaREEZr_2Ti_3Me^{3+}O_{14}$ – $Ca_2Zr_2Ti_2Me^{5+}Me^{3+}O_{14}$ without a need to involve the ideal zirconolite formula $Ca_2Zr_2Ti_4O_{14}$. The redefined composition space constrained by endmembers from this set, together with ideal

zirconolite, is suggested to be representative of the vast majority of more than 450 published zirconolite compositions worldwide with Me^{2+} + Me^{3+} totaling ≤1 atom per 14 O. The equation $X_{Me3+} = 2 - 2\ X_{REE*} - 3\ X_{Me5+*}$ provides an independent calculation of iron oxidation state or $X_{Me3+} = Me^{3+}/(Me^{2+} + Me^{3+})$ for this remarkable group of zirconolites, where X_{REE*} is derived from $X_{REE} = REE/(REE + Ca)$ and X_{Me5+*} from $X_{Me5+} = Me^{5+}/(Me^{5+} + Ti)$. Understanding the oxidation state of iron in zirconolite may be helpful to characterize redox conditions during its crystallization.

Keywords: zirconolite, stefanweissite, nöggerathite, polymignyte, Larvik Plutonic Complex, metamict, endmember, composition space, substitution, Rietveld refinement

INTRODUCTION

Alkaline pegmatites of Larvik Plutonic Complex in Norway are known to host numerous occurrences of zirconolite (e.g., Brøgger 1890; Larsen 2010; Piilonen et al. 2012; Andersen et al. 2013). The local variety of zirconolite from Fredriksvärn (called Stavern since 1930) was originally described by Jöns Jacob Berzelius in 1824 and named *polymignyte*. It was the very first discovered zirconolite worldwide, many decades earlier than the name zirconolite was given to a mineral with a similar composition from Afrikanda, Kola Peninsula in Russia (Borodin et al. 1956). Despite the chronological significance of *polymignyte*, the original term is no longer used and was replaced by the name zirconolite, according to the valid nomenclature (Bayliss et al. 1989). Zirconolite was favored because its use had become more frequent among mineralogists and nuclear waste scientists. Until this rationalization, minerals of similar appearance and composition were ambiguously labelled *polymignyte*, zirconolite or zirkelite. Such confusion resulted from several factors. Firstly, these phases usually show highly complex chemical compositions related to the ability of the minerals to accommodate wide ranges of chemical

constituents, often in high concentrations. Secondly, radioactive elements Th and U are commonly incorporated during mineral formation. Elevated concentrations of these alpha emitting elements coupled with increasing geological age give rise to partial or complete damage of the crystal structure, preventing identification of the mineral by means of X-ray diffraction techniques. Furthermore, metamictized crystals of the minerals showed diverse external morphologies and symmetries, being described as prismatic – (pseudo)orthorhombic, monoclinic, (pseudo)hexagonal, trigonal or cubic (Bayliss et al. 1989 and references therein).

Pioneering works dealing with description and refinement of crystal structures of crystalline — particularly synthetic or relatively rare natural phases with stoichiometries close to $CaZrTi_2O_7$ by Rossell (1980), Gatehouse et al. (1981), Sinclair and Eggleton (1982), Mazzi and Munno (1983) and White (1984) revealed polytypic behavior and distinguished monoclinic, orthorhombic and trigonal polytypes (or polytypoids) all being derived from an anion-deficient fluorite structure type (Rossell 1980). Based on these studies, Bayliss et al. (1989) assigned the names zirconolite-2*M* (aristotype), zirconolite-3*O* and zirconolite-3*T* to the crystalline minerals according to the symmetries and stacking (displacement and rotation) of their two kinds of internal layers. The first kind consists of HTB-like (hexagonal tungsten bronze) rings of TiO_6 octahedra enclosing split sites, statistically occupied by TiO_5 or TiO_4 polyhedra. These layers alternate with planes comprising chains of 8- and 7-fold coordinated Ca and Zr atoms, respectively (Mazzi and Munno, 1983; White 1984). Unlike the lower symmetry phases, the mineral with a cubic symmetry does not show a layered structure and was given a separate name, zirkelite. Metamict zirconolite-related minerals, the original structure of which is uncertain, should be called zirconolite (Bayliss et al., 1989).

In terms of chemical composition, natural zirconolite commonly deviates from its ideal formula $CaZrTi_2O_7$ (Williams and Gieré 1996; Gieré et al. 1998). Calcium may be substituted by variable

amounts of yttrium and lanthanides (≤70–80 mol% of the M[VIII] sites; Harley 1994; Rasmussen et al. 2008; Sharygin 2014), uranium and thorium (≤30–40 mol%; Gieré and Williams 1992; Rajesh et al. 2006; Čopjaková et al. 2008; Čopjaková and Houzar 2009; Hurai et al. 2018), divalent cations – particularly manganese (≤10–20 mol%; Della Ventura et al. 2000; Chukanov et al. 2014, 2018, 2019), or magnesium. Octahedral sites are commonly enriched in Nb (≤0.7–0.9 atoms per 7 O; Borodin et al. 1960; Sinclair and Eggleton 1982; Keller 1984; Bulakh et al. 1999; Della Ventura et al. 2000; Chukanov et al. 2014, 2018, 2019) accompanied by moderate Ta contents (≤0.07 apfu). Less frequently, the sites are found to contain, low amounts of W (Gieré and Williams 1992) or Zr (Williams and Gieré 1996). Divalent and trivalent metals, particularly Fe and subordinate Mg, Mn, Al, and rarely Cr, may participate at the expense of Ti (≤0.6 apfu), but preferably in the split sites. Incorporation of these elements into octahedral sites is limited (e.g., Mazzi and Munno 1983; Chukanov et al. 2014, 2018, 2019; Zubkova et al. 2018). Elevated Fe contents approaching 1 atom per 7 O and significant participation of the element in one of the two distinct octahedral sites (increasing with overall iron content) separately from the split site may occur in synthetic zirconolite (e.g. Whittle et al. 2012).

Contents of Zr show relatively low scatter and are close to the ideal value of 1 apfu. This element is commonly substituted by small amounts of Hf (≤0.03 apfu). Elevated contents of Zr (≥1.2 apfu) were reported by Lorand and Cottin (1987), while Zr-depleted compositions (≤0.9 apfu) were observed by Della Ventura et al. (2000), Carlier and Lorand (2008) or Hurai et al. (2018).

Based on the extensive set of chemical analyses of natural zirconolite worldwide (Williams and Gieré 1996), Gieré et al. (1998) constrained a composition space comprising of ideal zirconolite and 4 more linearly independent hypothetical endmembers ($ACTZrTiMe^{2+}O_7$, $REEZrMe^{5+}Me^{2+}O_7$, $CaZrMe^{5+}Me^{3+}O_7$, $REEZrTiMe^{3+}O_7$, where $ACT=U^{4+}+Th^{4+}$,

REE=Y+lanthanides, Me^{5+}=Nb+Ta, Me^{2+}=Fe^{2+}+Mg+Mn and Me^{3+}=Fe^{3+}+Al), which was assumed to be representative of the vast majority of natural zirconolite compositions.

Recently, new crystalline analogs of zirconolite-*3O* called laachite – $Ca_2Zr_2Nb_2TiFe^{2+}O_{14}$, stefanweissite – $(Ca,REE)_2(Zr,Mn)_2(Ti,Nb)_2(Nb,Ti)Fe^{2+}O_{14}$ and nöggerathite – $(REE,Ca)_2(Zr,Mn)_2(Ti,Nb)_2(Nb,Ti)Fe^{2+}O_{14}$ were described from Laacher See, Germany (Chukanov et al. 2014, 2018, 2019) and approved as new minerals. However, the relationships of these new minerals to the composition space suggested by Gieré et al. (1998) has not been clarified.

Our study is focused on zirconolite from alkaline pegmatites of the Larvik Plutonic Complex, Norway, the region of the original *polymignyte* discovery. Chemical compositions of four metamict crystals from 3 localities (Håkestad, Stålaker and Agnes) were determined by means of electron probe microanalysis. In the case of zirconolite from Håkestad, Mössbauer spectroscopy was used to quantify oxidation state of iron and X-ray powder diffraction (XRPD) was used to study the effect of thermal annealing on initially damaged zirconolite structure. The results reveal a link between the classic "*polymignytes*" and the newly approved minerals stefanweissite and nöggerathite (Chukanov et al. 2018, 2019). Moreover, our data are helpful to explain the somewhat unclear relationship between the newly approved minerals from Laacher See described by Chukanov et al. (2014, 2018, 2019) and the endmember set of Gieré et al. (1998). In addition, we have identified a new zirconolite endmember that may also be involved in previously published compositions. Based on this careful analysis of the composition space, we suggest modified endmember systematics, which correspond well to most known zirconolite compositions worldwide and provides a necessary extension of the composition space constrained by Gieré et al. (1998). In accordance with this new endmember system, we present an

approach to easily estimate iron oxidation state from other composition variables and discuss possible implications of this approach.

GEOLOGICAL SETTINGS AND HOST PEGMATITES

The Larvik Plutonic Complex (LPC) is situated at the southern part of the Oslo Paleorift (see e.g., Larsen et al. 2008) and comprises 10 circular plutons (Petersen 1978) composed particularly of regionally specific varieties of monzonitic rocks called larvikites and less abundant nepheline syenites (Neumann 1980; Rasmussen et al. 1988; Dahlgren 2010). Spatial relationships among plutons (Petersen 1978) as well as U-Pb isotopic dating of zircon and baddeleyite from the rocks indicate decreasing age from the easternmost and oldest quartz-bearing larvikites (298.6±1.4 Ma according to Dahlgren et al. 1996; 298±0.4 Ma according to Rämö and Andersen 2011), through the central quartz- and nepheline-free larvikites, to the youngest nepheline-bearing larvikites and syenites (292.1±0.8 Ma according to Dahlgren et al. 1996; 289.7±0.5 Ma according to Rämö and Andersen 2011) at the western part of the complex. Larvikites host numerous bodies of alkaline pegmatites emplaced soon after solidification of the hosts (Sunde et al. 2019). Both rock types are assumed to share a common magmatic source (Sunde et al. 2018). The occurrence of zirconolite is distinctive for miaskitic pegmatites (Andersen et al. 2013) in contrast to the more complex and strongly alkaline agpaitic pegmatites (e.g., Andersen et al. 2010). Furthermore, alkalinity is a key factor of regional alkaline pegmatite typology (e.g., Piilonen et al. 2012, 2013; Sunde et al. 2019) regarding mineral assemblages and shapes of pegmatites from the LPC. The Håkestad and Stålaker quarries are situated within ring sector 5 of the LPC (see e.g., Petersen 1978; Dahlgren 2010), about 500 m apart, and approximately 5 km northeast of the town of Larvik, Vestfold district, Norway. The zirconolite-bearing, coarse grained pegmatites occur as lenses in larvikite. The major minerals of the pegmatites are cryptoperthitic feldspar, nepheline, hastingsitic

amphibole, biotite, magnetite, zircon, pyrochlore and zirconolite. The Agnes (Tronsrødfjellet) locality is a roadcut where the pegmatite was exposed during expansion of the RV 301 road (Larviksveien) in the 1970's and occurs in ring sector 6 of the LPC. The pegmatite is relatively fine-grained and contains slightly altered cryptoperthitic feldspar, amphibole, magnetite, zircon and zirconolite. Small vugs in the pegmatite are lined with analcime overgrown by catapleiite and calcite. Our studied zirconolite from the 3 localities was surrounded by albite and occurs as black to dark brown prismatic crystals with a sub-metallic luster ranging from c. 1 cm to several centimeters in length.

ANALYTICAL TECHNIQUES

X-ray Powder Diffraction

The variable-temperature XRPD was measured using an X`Pert PRO MPD powder diffractometer (PANalytical) in combination with mounted reaction chamber XRK900 (Anton Paar) at the Regional Centre of Advanced Technologies and Materials at Palacký University, Olomouc. The diffractometer operates in Brag-Brentano geometry and is equipped with a Co K_α radiation source, a position sensitive X`Celerator detector, and programmable divergence and diffracted beam antiscatter slits. The diffraction patterns were captured at 2θ range from 15 to 90° (2θ resolution of 0.0167°, collection time of 60 minutes). The progressive heating of the zirconolite (grounded under isopropyl alcohol to avoid iron oxidation) from Håkestad was performed in a nitrogen atmosphere with collection of 10 XRPD patterns at each selected temperature (i.e., at room temperature, 400, 600, 800 and 900 °C). The commercially available standards SRM640 (Si) and SRM660 (LaB_6) were used for evaluation of the line positions and experimental line broadening, respectively. The initial identification of the relevant structure types was carried out using High Score plus software in conjunction with PDF-4+, ICSD and

COD databases. Rietveld refinement of the acquired XRPD data has been conducted using computer program JANA2006 (Petříček et al. 2014) to identify the potentially involved zirconolite polytypes and to quantify the relative amounts and the unit cell parameters of the identified phases. The examined scenarios were based on structural models of cubic ZrO_2 (Wyckoff 1963) and different zirconolite polytypes (Rossell 1980; Mazzi and Munno 1983; Grey et al. 2003; Whittle et al. 2012; Zubkova et al. 2018; Chukanov et al. 2019), with fixed atomic parameters and unit cell parameters allowed to refine.

Electron probe microanalysis (EPMA)

Chemical analyses of zirconolite were measured with the electron microprobe Cameca SX100 at the Department of Geological Sciences, Faculty of Science at the Masaryk University, Brno, Czech Republic. An accelerating voltage of 15 kV and an electron beam defocused to 3 μm in diameter with a current of 20 nA were applied. Following monochromators, X-ray lines and standards were used during the WDS analyses: TAP: Na K_α (albite), Zr L_α (zircon), Hf M_α (Hf), Y L_α (YPO_4), Mg K_α (Mg_2SiO_4), Si K_α (zircon), Sr L_α ($SrSO_4$), Al K_α (sanidine); PET: Ti K_α ($SrTiO_3$), La L_α ($LaPO_4$), Ce L_α ($CePO_4$), P K_α ($LaPO_4$); LLIF: Fe K_α (columbite), Mn K_α (Mg_2SiO_4), Pr L_β ($PrPO_4$), Nd L_β ($NdPO_4$), Sm L_α ($SmPO_4$), Gd L_β ($GdPO_4$), Dy L_β ($DyPO_4$), Er L_α ($ErPO_4$), Yb L_α ($YbPO_4$); LPET: Ca K_α (fluorapatite), Nb L_α (columbite), U M_β (U), Th M_α ($CaTh(PO_4)_2$), Pb M_β ($PbSiO_3$), W M_α (W), Ta M_α ($CrTa_2O_6$); PC1: F K_α (topaz). Raw measured data were corrected for matrix effects using X-Phi procedure of Merlet (1994). Spectral interferences of Nb on Y L_α, Er on Si K_α, Nd on SiK_α and Gd L_α, Ta on Zr L_α, and Ce on F K_α were corrected using empirical correction factors. Concentrations of Na, Al, Sr, P, F and W did not exceed detection limits ranging from 200 to 900 ppm.

Mössbauer Spectroscopy

The transmission ^{57}Fe Mössbauer spectrum of original unannealed zirconolite (grounded under isopropyl alcohol to avoid iron oxidation) from Håkestad was collected using a MS96 spectrometer run in constant acceleration mode at room temperature with a ^{57}Co(Rh) radioactive source (1.85 GBq) at the Regional Centre of Advanced Technologies and Materials at Palacký University, Olomouc. The values of hyperfine parameters (i.e., isomer shift values) were calibrated against a rolled metallic iron (α-Fe) foil. The spectrum was fitted with Lorentz functions using the CONFIT2000 software. The experimental error was ±0.02 mm s^{-1} for the hyperfine parameters and ±3% for the relative spectral areas. The measured spectrum and its quantitative parameters are attached as Fig. A1 and Tab. A1 in Appendix A.

RESULTS

High-temperature X-ray powder diffraction

X-ray powder diffraction pattern of unannealed zirconolite from the Håkestad quarry (Fig. B1 in Appendix B) shows a single broad Gaussian-shape background feature centered at c. 38° 2θ, demonstrating the metamict state of the mineral. Annealing at 400 °C initialized recrystallization which formed three very weak peaks accompanied by weakening of the broad relict of the former amorphous state. Intensities of newly formed peaks increased under 700–800 °C. At 800 °C, the peaks were centered at 35.35°, 41.04°, 59.46°, 71.12° and 74.82° 2θ while the original broad feature completely disappeared. This X-ray diffraction pattern (Fig. 1a) corresponds to a pattern of a cubic ZrO_2 (Wyckoff 1963) with a space group *Fm-3m* and the refined unit cell parameters: a = 5.1047(4) Å, V = 133.02(2) Å^3. Further annealing at 900 °C induced a phase transition that caused splitting of the major peaks observed in the previous patterns into additional sharper diffraction maxima (Fig. B1 in Appendix B). After cooling the sample to room temperature, their

positions slightly shifted towards higher 2θ due to volume reduction (Fig. 1b). Two phases – zirconolite-*3O* (space group *Cmca*) and zirconolite-*3T* (space group $P3_121$) participate in the final Rietveld fit (Fig. 1b). Structural models of stefanweissite (Chukanov et al. 2019) and zirconolite-*3T* (Zubkova et al. 2018) were found to properly represent final scattering power at mixed sites of different Wyckoff positions in the studied material and were used in the refinement. Weight fractions of 0.612(4) and 0.388(5) were obtained for the two phases. The refined unit cell parameters are: a = 7.2664(8) Å, b = 14.1877(15) Å, c = 10.1472(12) Å, V = 1046.1(2) Å^3 for the orthorhombic and a = 7.2766(6) Å, c = 17.0627(15) Å, V = 752.42(11) Å^3 for the trigonal structural type.

Chemical composition of zirconolite

Electron probe imaging (Fig. 2) and microanalyses revealed certain similarities among the studied grains from all the three localities. Individual grains of zirconolite from Håkestad and Stålaker are characterized by relatively limited compositional heterogeneity with a very smooth change of chemical compositions between center and rim. The BSE zoning is mostly weak to negligible, although two distinct growth zones may be distinguished in some parts, as seen in Fig. 2a. In contrast, BSE imaging of Agnes zirconolite display more significant patchy zoning with sharp transition between brighter and darker areas (Fig. 2b). As demonstrated below, the zoning is mainly related to differences in actinide contents.

Ideal zirconolite contains 16.54 wt% CaO, 36.34 wt% ZrO_2, and 47.12 wt% TiO_2. All investigated grains in our study are significantly depleted in the major components (5.88–7.85 wt% CaO, 27.01–28.76 wt% ZrO_2, 17.15–20.93 wt% TiO_2) compared to ideal zirconolite (Tab. 1). Conversely, all of them are strongly enriched in Nb_2O_5 (11.13–17.25 wt%), REE_2O_3 (10.75–18.73 wt%), FeO* (7.78–8.88 wt%, where FeO* represents hypothetical FeO equivalent to

measured Fe), ThO_2 (2.55-5.22 wt%), UO_2 (0.64–2.46 wt%) and Ta_2O_5 (0.74–1.23 wt%). The concentrations of MnO, MgO, HfO_2, SiO_2, and PbO are always lower than 1 wt%. Analytical totals range between 97 and 99 wt%.

Two separate grains from the Håkestad quarry show somewhat variable contents of Nb_2O_5 (11.49–17.25 wt.), TiO_2 (17.43–20.93 wt%), ThO_2 (2.55–5.10 wt%) and UO_2 (0.65–2.14 wt%). Compared to other samples, concentration of REE_2O_3 (11.22–14.87 wt%) is relatively low to intermediate. Based on Mössbauer spectroscopy, the ratio of $X_{Fe3+} = Fe^{3+}/Fe_{tot}$ in zirconolite from Håkestad is 0.206 ± 0.024.

Zirconolite from Stålaker quarry is the richest in REE (14.51–18.73 wt% REE_2O_3) among the three localities. In contrast, the TiO_2 (17.15–17.74 wt%), ZrO_2 (27.01–27.68 wt%) and CaO (5.88–6.55 wt%) contents are the lowest.

When compared to all other localities, the sample from the Agnes quarry is the richest in UO_2 (1.38–2.46 wt%, with the highest U/Th ratio), while Nb_2O_5 range from the lowest to intermediate values (11.13–15.11 wt%). Contents of other components fall within ranges observed in the other two localities.

Rare earth elements

Contents of rare earth element oxides are shown in Tab. 1. Cerium (4.86 ± 0.8 wt%), Nd (2.39 ± 0.28 wt%), Y (1.26 ± 0.19 wt%) and La (1.17 ± 0.27 wt%) are the most abundant REE's exceeding 1 wt%. As seen in Fig. 3, shapes of chondrite-normalized (McDonough and Sun 1995) patterns representing samples from all studied localities are very similar. Differences in overall REE contents among the samples slightly influence the shift of the whole pattern along the vertical axis rather than their shapes. The patterns are convex between La and Dy with maxima at Ce and Pr followed by a smooth decrease towards heavier elements, while the slope become quite

horizontal between Dy and Yb with a slight to negligible negative yttrium anomaly ($Y/Y^*=Y_N/(Dy_N \times Er_N)^{0.5}$) of 0.72–0.91. The enrichment of LREE relative to HREE can be approximately expressed as a ratio of $(Ce_N+Nd_N)/(Gd_N+Dy_N)$, which is 3.5–7.2.

Crystal-chemical formulae and site occupancy

The vast majority of crystal-chemical formulae of zirconolite published in literature are based on 4 cations and/or 7 oxygen atoms, which are in agreement with reviews of Williams and Gieré (1996) or Gieré et al. (1998). By contrast, formulae in Tab. 2 of Bayliss et al. (1989), formulae in Mazzi and Munno (1983) or those of new zirconolite analogs from Laacher See introduced by Chukanov et al. (2014, 2018, 2019) and zirconolite-*3T* of Zubkova et al. (2018) are calculated to give a sum of 14 oxygens. The fivefold- or fourfold-coordinated cations, Me^{2+} and Me^{3+}, yield a sum of approximately 1 apfu in the minerals from Laacher See. Given that the data in our study are extensively compared with compositions published by Chukanov et al. (2014, 2018, 2019) the latter normalization approach is adopted in this study: cations give a sum of 8 apfu and Fe^{3+} versus Fe^{2+} proportions are given by balancing charges to a sum of 28 (14 O apfu; Tab. 1). Calculated values of Fe^{3+}/Fe_{tot} for the Håkestad zirconolite (0.16 ± 0.03) are in good agreement with the value of 0.206 ± 0.024 obtained from Mössbauer spectroscopy. For samples from Stålaker and Agnes, the charge-balance-based ratios are 0.12 ± 0.03 and 0.14 ± 0.04, respectively. Divalent Fe in all samples is thus assumed to strongly predominate over trivalent. Gieré et al. (1998) allocated cations into 3 site types. We adopted their approach (except for Mn; Tab. 1) as follows: M[VIII] sites (totaling 2 apfu) were filled with Ca, REE, U, Th; Pb is assumed to be exclusively radiogenic decay product of the actinides (Gieré et al. 1998; our unpublished LA-ICP-MS isotopic data); M[VII] sites (2 apfu) were filled with Zr, Hf and Mn; M[VI,V, IV] (4 apfu) sites were filled with Ti, Nb, Ta, Fe, Mg and Si. Manganese concentrations in natural

zirconolite (e.g. compilation of Williams and Gieré 1996) rarely exceed those measured in our samples (0.53–0.93 wt% MnO; 0.06–0.11 atoms per 14 O). Uncommon, Mn-rich compositions (2–9.4 wt% MnO) from Laacher See were reported for zirconolite-3*O* and its analogs laachite, nöggerathite and steffanweissite (Della Ventura et al. 2000; Chukanov et al. 2014, 2018, 2019). Based on single-crystal X-ray diffraction data acquired from type laachite, Chukanov et al. (2014) allocated Mn preferentially into the M[VII] site in their structural model. Moreover, the M[VII] site was occupied by a certain fraction of manganese also in structural models of the type stefanweissite and nöggerathite (Chukanov et al. 2018, 2019). We observe a trend of slightly increasing Mn with moderately decreasing Zr in our data, but the correlation coefficient is relatively poor (R^2=0.53) due to very limited compositional ranges of both elements. Furthermore, allocation of Mn into M[VII] gives all site subtotals close to ideal values. By contrast, allocation of Mn into the nominally Ti-bearing, M[VI,V,IV] would systematically overfill these sites.

Håkestad. According to our crystal-chemical model, occupancy of M[VIII] site is 1.930–2.002 apfu with 1.068–1.154 Ca apfu, 0.640–0.750 REE apfu, 0.106–0.218 ACT + Pb apfu and Th/U between 2.7 and 4.3. The sum of Zr (1.882–1.946 apfu), Hf (0.008–0.018 apfu) and Mn (0.072–0.106 apfu) give the M[VII]-site subtotal of 1.998–2.030. The M[VI,V,IV] sites have a subtotal of 3.984–4.060 apfu comprised of 1.856–2.216 Ti apfu, 0.754–1.104 Nb apfu, 0.038–0.044 Ta apfu, 0.976–1.006 Fe apfu and 0.012–0.036 Mg apfu.

Stålaker. Zirconolite from Stålaker give a subtotal of M[VIII] site between 1.980 and 2.030. In addition, the analyses show relatively high REE (0.876–0.926 apfu), contrary to relatively low Ca (0.908–1.008 apfu) and ACT (0.082–0.116 apfu Th, 0.020–0.044 apfu U; 0.108–0.164 ACT + Pb; Th/U = 2.6–4.1) in this site. Zirconium (1.888–1.940 apfu), hafnium (0.018–0.022 apfu) and manganese (0.076–0.086) give the M[VII] a subtotal of 1.986–2.034. The subtotal of the

M[VI,V,IV] sites are 3.972–4.003 apfu. The presence of titanium predominates even though its content, unlike in the other localities, ranges below 2 apfu (1.816–1.912 apfu). Significant Nb content (0.916–1.052 apfu) is accompanied by subordinate Ta (0.028–0.048 apfu). Iron and Mg yield 1.034–1.068 and 0.024–0.044 apfu, respectively.

Agnes. The M[VIII] site subtotal is 1.950–2.014 apfu. It contains 0.990–1.188 Ca apfu, 0.676–0.776 REE apfu, 0.100–0.170 Th apfu, 0.044–0.078 U apfu and shows a relatively low Th/U ratio (2.15–2.56). Zirconium (1.908–2.014 apfu) and Hf (0.016–0.028 apfu) give a M[VII]-site subtotal of 2.001–2.156 apfu. In comparison with other samples, contents of pentavalent cations – Nb and Ta in M[VI,V,IV] are relatively low (0.722–0.964 apfu and 0.030–0.042, respectively). Conversly, Ti content is relatively high (1.974–2.232). Moreover, the M[VI,V,IV] sites giving subtotal of 3.842–4.038 comprise 0.936–0.984 Fe apfu and 0.010–0.044 Mg apfu.

Substitutional behavior and composition space

Among the chemical constituents of zirconolite, Ti and Me^{5+} are those with the most significant compositional variation (ΔTi = 0.360, 0.258 and 0.096 apfu; ΔMe^{5+} = 0.350, 0.242, 0.136 apfu in Håkestad, Agnes and Stålaker, respectively). The studied compositions show a well-defined negative correlation between Ti and Me^{5+} reflecting direct heterovalent interchange of these elements in the octahedral sites (Fig. 4a). Regarding spatial distribution of these elements, the ratio of $X_{Me5+} = (Me^{5+})/(Me^{5+}+Ti)$ increases from the center towards the rim of the metamictized crystals. In the case of Stålaker, X_{Me5+} is negatively correlated with X_{REE} = REE/(REE+Ca) having dX_{Me5+}/dX_{REE} slope of c. -0.77 (Fig. 4b). Nevertheless, the corresponding plot of data from Håkestad and Agnes shows a dramatic drop of X_{Me5+} with a relatively slight increase of X_{REE} and a steep dX_{Me5+}/dX_{REE} slope of <-4 (Fig. 4b). The relationship between these two compositional parameters is diagnostic for the two distinctly differing modes of substitutional

behavior observed in the studied zirconolite from Stålaker compared to Håkestad. Furthermore, Håkestad-type zirconolite shows rather constant content of $Me^{2+} + Me^{3+}$, while growth of $Me^{2+} + Me^{3+}$ with increasing ACT content (and decreasing X_{Me5+}) is observed in Stålaker-type zirconolite (Fig. 5b). Despite the relatively limited range of ACT contents, the significant increase of X_{Me5+} is strongly related to decreasing participation of actinides (Figs. 4b, 5). Regarding this obvious relationship, our models of substitutional behavior assume mixing between two composition subspaces: (A) an actinide-free subspace and (B) an actinide-enriched, Nb-free subspace.

Each of the two observed modes (Stålaker and Håkestad) aims toward one terminal composition in subspace (A) determined by extrapolation of compositional trends to zero actinide content (Fig. 6), and one terminal composition in subspace (B) given by extrapolation of observed compositional trends related to a growth of actinide contents until all Me^{5+} is substituted by Ti (Fig. 6c, d). Indeed, each of these terminal compositions (marked with triangles in Figs. 6, 7) are projected at one edge of either the Ca–ACT–REE or Ti–($Me^{2+} + Me^{3+}$)–Me^{5+} triangle (or both in the case of the Nb-free terminal composition of Stålaker type; see Fig. 7). Hereafter, these two outermost compositions are referred to as *"edgemembers"*, because they join 2 edges of the whole composition space.

Given that the relationship between ACT and charge-balance-based X_{Fe3+} values are highly uncertain, there were no persuasive clues of whether trivalent iron should be attributed to the *edgemember B* or to both *edgemembers*. As the cluster of Håkestad analyses with higher ACT content shows somewhat higher average X_{Fe3+} compared to the ACT-poor cluster (0.18>0.14), Fe^{3+} content is assumed to grow with increasing ACT and Fe^{3+} and therefore participates only in the *edgemember B*. Evolution of Mn (allocated in a 7-fold-coordinated site together with Zr) content as a function of increasing ACT is also unclear, but with a site occupancy of 5% or less

its influence on our models is limited. Based on these assumptions and the observed compositional trends, Håkestad-type *edgemembers A* and *B* were determined as follows: $Ca_{1.3}REE_{0.7}Zr_{1.9}Mn_{0.1}Ti_{1.5}Me^{5+}_{1.5}Me^{2+}O_{14}$ and $Ca_{0.8}REE_{0.7}ACT_{0.5}Zr_{1.9}Mn_{0.1}Ti_3Me^{2+}_{0.5}Me^{3+}_{0.5}O_{14}$, respectively. Due to this simplification involving mixing of only two components, a general substitution vector **ACT + 3Ti + Me^{3+} = Ca + 3Me^{5+} + Me^{2+} (**depicted by violet line segments in Figs. 6, 7), can be determined simply from the difference between the two *edgemembers*. The vector fits well with the measured data from the Håkestad and Agnes zirconolite (Fig. 6).

The *edgemember A* of Stålaker-type, $Ca_{1.2}REE_{0.8}Zr_{1.95}Mn_{0.05}Ti_{1.7}Me^{5+}_{1.3}Me^{2+}O_{14}$, is relatively similar to the previous Håkestad type, whereas *edgemember B*, $ACT_{0.7}REE_{1.3}Zr_2Ti_{2.6}Me^{2+}_{0.7}Me^{3+}_{0.7}O_{14}$, differs considerably from that of Håkestad type. More significant growth of X_{REE} in Stålaker type is related to substantial enrichment in REE along with loss of Ca, the content of which would be zero at the Nb-free (and Ca-free) composition of *edgemember B* (Figs. 6a, b, 7). On the other hand, a moderate increase of X_{REE} in the previous Håkestad type is related to substitution of ACT for Ca at rather constant REE (Fig. 6a, b). In addition, *edgemember B* of Stålaker type must contain more than 1 atoms Me^{2+}+Me^{3+} per 14 O to reflect the increasing (Me^{2+}+Me^{3+})/(Me^{2+}+Me^{3+}+Ti+Me^{5+}) ratio with growing participation of ACT (Fig. 6e). The determined general substitution vector **0.7 ACT + 0.5 REE + 0.9 Ti + 0.7 Me^{3+} + 0.05 Zr = 1.2 Ca + 1.3 Me^{5+} + 0.3 Me^{2+} + 0.05 Mn** (brown line segments in Figs. 6, 7) corresponds reasonably well to the observed evolution of zirconolite from Stålaker (Figs. 5, 6).

Endmember fractions

Gieré et al. (1998) reported 5 independent endmembers which are assumed to participate in natural zirconolite compositions. Following the formalism used in this study, their formulae can be expressed as follows: $Ca_2Zr_2Ti_4O_{14}$ (ideal zirconolite), $ACT_2Zr_2Ti_2Me^{2+}_2O_{14}$,

$REE_2Zr_2Me^{5+}{}_2Me^{2+}{}_2O_{14}$, $REE_2Zr_2Ti_2Me^{3+}{}_2O_{14}$, $Ca_2Zr_2Me^{5+}{}_2Me^{3+}{}_2O_{14}$. More recently described crystalline analogs of zirconolite-*3O*: laachite – $Ca_2Zr_2Nb_2TiFe^{2+}O_{14}$, nöggerathite – $(REE,Ca)_2Zr_2(Nb,Ti)(Ti,Nb)_2Fe^{2+}O_{14}$ and steffanweissite – $(Ca,REE)_2Zr_2(Nb,Ti)(Ti,Nb)_2Fe^{2+}O_{14}$ (Chukanov et al. 2014, 2018, 2019) are characterized by preferential ordering of Ti and Nb in octahedral sites and occupation of the split sites solely by Fe ± Mn (the ratio of $Fe/(Fe+Ti+Me^{5+})$ is very close to 0.25). Unfortunately, such detailed structural data are rarely available. Moreover, the two latter minerals are not defined by fixed chemical formulae, which is the first condition an endmember formula should meet according to Hawthorne (2002). This precludes quantification of endmember fractions if such compositions are to be considered. Nevertheless, reported compositions of natural steffanweissite (Ca-dominant) and nöggerathite (REE-dominant) are relatively close to an intermediate charge-balanced formula $CaREEZr_2Ti_2Me^{5+}Me^{2+}O_{14}$. Although the definition of the two recently approved minerals from Laacher See are ambiguous in terms of participating endmembers, the above suggested intermediate formula is similar to one of the formulae Chukanov et al. (2019) considered to represent nöggerathite. It is noteworthy that this formula is not linearly independent of the original set of Gieré et al. (1998) and can be obtained by a combination of ideal zirconolite, $Ca_2Zr_2Ti_4O_{14}$ and $REE_2Zr_2Me^{5+}{}_2Me^{2+}{}_2O_{14}$. This linearly dependent intermediate endmember shows equal contents of Ca and REE in the M[VIII] sites and 1 apfu of Nb and 2 apfu of Ti occupying octahedral sites totaling 3 apfu. If ordering of Ti and Nb is assumed, such configuration agrees with the definition of nöggerathite and steffanweissite, both having "Nb prevailing over Ti in one octahedral site" (Chukanov et al. 2018, 2019).

As we mentioned above, the role of Mn in crystal chemistry of our zirconolite is relatively minor (up to 0.11 atoms per 14 O) and somewhat unclear. Keeping this in mind, arbitrary $^{[VII]}Mn$-bearing endmembers derived from the above-mentioned endmembers are included in our

expression in order to (i) achieve full compatibility between the two-component (*edgemember*-) mixing model and the model of participating endmembers, (ii) maintain the electroneutrality of simulated compositions, (iii) maintain ideal zirconolite stoichiometry and site allocations as described above.

Quantification of endmember fractions in such complex systems is always arbitrary and the results may strongly depend on a chosen set of endmembers as well as on the order and means of component extraction if the sequential approach (Rickwood 1968; Della Ventura et al. 2000; Hurai et al. 2018) is adopted or if the endmember formulae are mutually convertible within a reciprocal composition system (e.g., Dolivo-Dobrovol´sky 2010). This is the case of the studied system as shown below. Endmember fractions in our study are calculated from the simulated compositions rather than from the measured compositions, but are well representative for the latter, as the simulated compositions are based on and agree with the observed compositional trends (Figs. 5, 6, 7). The advantage of this approach is that it depicts a continuous change as a function of mineral zoning, reflects compositional trends of the whole population, and enables extrapolation beyond the observed compositions.

Compositions of our *edgemembers A* are very close to the $Ca_2Zr_2Me^{5+}{}_2TiMe^{2+}O_{14}$ – $CaREEZr_2Ti_2Me^{5+}Me^{2+}O_{14}$ binary. Håkestad-type *edgemember A* composition is attained by a mixture of 36.5 mol. % $Ca_2Zr_2Me^{5+}{}_2TiMe^{2+}O_{14}$ and 57% $CaREEZr_2Ti_2Me^{5+}Me^{2+}O_{14}$ giving subtotal of 93.5%, while 23.33% $Ca_2Zr_2Me^{5+}{}_2TiFe^{2+}O_{14}$ and 73.33% $CaREEZr_2Ti_2Me^{5+}Me^{2+}O_{14}$ give 96.7% of the *edgemember A* of Stålaker zirconolite. The remaining 6.5% and 3.3%, respectively, are contributed by an arbitrary $^{[VII]}$Mn-bearing $REE_2Zr_{0.5}Mn_{1.5}Nb_3Me^{2+}O_{14}$ derived from $REE_2Zr_2Ti_3Me^{2+}O_{14}$. To simulate the compositions of *edgemembers B*, endmembers containing ACT and Fe^{3+} must be involved, while Nb-bearing (and Ca-bearing in the case of the Stålaker locality) must be excluded. Furthermore, in Håkestad-type *edgemember B* the ratio of

$(Me^{2+} + Me^{3+})/(Me^{2+} + Me^{3+} + Ti + Me^{5+})$ is fixed at a value of 0.25 (Figs. 5, 6, 7). Such behavior may be simulated by careful coupling of endmembers from Gieré et al. (1998) having $(Me^{2+} + Me^{3+})/(Me^{2+} + Me^{3+} + Ti + Me^{5+}) = 0.50$ with ideal zirconolite to give linearly dependent endmembers showing the required stoichiometry: 50% $CaACTZr_2Ti_3Me^{2+}O_{14}$ (given by $ACT_2Zr_2Ti_2Me^{2+}{}_2O_{14}$ + $Ca_2Zr_2Ti_4O_{14}$) + 30% $CaREEZr_2Ti_3Me^{3+}O_{14}$ (given by $REE_2Zr_2Ti_2Me^{3+}{}_2O_{14}$ + $Ca_2Zr_2Ti_4O_{14}$) and 20% arbitrary $REE_2Zr_{1.5}Mn_{0.5}Ti_3Me^{3+}O_{14}$ (i.e. derivative of $REE_2Zr_2Ti_2Me^{3+}{}_2O_{14}$). The Stålaker-type *edgemember B* composition lacks such coupling and comprises 35% $ACT_2Zr_2Ti_2Me^{2+}O_{14}$, 35% $REE_2Zr_2Ti_2Me^{3+}O_{14}$, and 30% arbitrary $REE_2ZrMnTi_4O_{14}$ (yielded from $REE_2Zr_2Ti_2Me^{3+}O_{14}$).

Figure 8 shows calculated endmember fractions as a function of either mixing ratio of the *edgemember B* composition (primary x-axis) or actinide content (secondary x-axis). The compositional ranges observed in our data are accentuated. The relationships between the linearly independent and the linearly dependent endmembers are also demonstrated. If a set comprising laachite (red field in the figure) and independent endmembers, i.e. ideal zirconolite (all orange fields) and endmembers of Gieré et al. (1998) (other colors) are chosen to describe the relevant part of the composition space, our observed Håkestad-type compositions yield an ideal zirconolite fraction of c. 31–34%. Alternatively, contribution of 18–29% laachite and 29–46% $CaREEZr_2Ti_2Me^{5+}Me^{2+}O_{14}$ may be extracted from a bulk composition giving 8–20% ideal zirconolite (orange fields with patterns of dashes and crosshairs). Nevertheless, this fraction of ideal zirconolite must be coupled with other independent endmembers to keep the bulk $(Me^{2+} + Me^{3+})/(Me^{2+} + Me^{3+} + Me^{5+} + Ti)$ ratio equal to 0.25. Therefore, the fraction of ideal zirconolite is zero if the bulk composition is expressed by means of the ACT-, REE- and Fe^{3+}-bearing linearly dependent endmembers (patterns in Fig. 8).

DISCUSSION

Alpha-decay damage, thermal annealing and characterization by means of X-ray powder diffraction

The initial XRPD pattern of investigated zirconolite from Håkestad lacked any characteristic diffraction maxima (Fig. B1 in Appendix B). Such a pattern is symptomatic of a crystal structure that has been completely damaged by self-irradiation induced by alpha decay of thorium and uranium incorporated during mineral formation. Based on the measured actinide contents and approximate geological age of 295 Ma (Dahlgren et al. 1996; Rämö and Andersen 2011; our unpublished data), the accumulated radiation dose is calculated after Holland and Gottfried (1955), (see also Lumpkin et al. 1997) to achieve values of 1.06–2.48×10^{16} α-decays/mg in the Håkestad zirconolite, 1.77–3.10×10^{16} α-decays/mg in Agnes zirconolite and 1.05–1.85×10^{16} α-decays/mg in the Stålaker zirconolite. Even the lowest of these values exceed the range of c. 0.05–0.90×10^{16} α-decays/mg at which the crystalline-amorphous transformation of natural as well as of synthetic, short-lived actinide-doped zirconolite, takes place (Lumpkin et al. 1986; Weber et al. 1986; Clinard et al. 1991; Lumpkin et al. 1997). Our X-ray powder diffraction data are thus in agreement with these works. Like this study, Lumpkin et al. (1998) investigated radiation damage of zirconolite from the LPC, Norway, and reported doses reaching 4.4×10^{16} α-decays/mg for most actinide-rich samples, while relics of crystallinity were preserved in some actinide-depleted samples which absorbed doses as low as c. 0.1×10^{16} α-decays/mg. Furthermore, some zirconolite specimens from different and older terranes remained partially crystalline even though they were exposed to doses exceeding 10^{16} α-decays/mg, due to long-term thermal annealing (Lumpkin et al. 1998). However, remarkable structure recovery and substantial increase of critical amorphization dose associated with such process is relatively moderate in zirconolite younger than c. 300 Ma (Lumpkin et al. 1998, their Fig. 2). Therefore, long-term thermal annealing is

assumed to be rather ineffective in zirconolite from the LPC, and all samples described in this study are very likely entirely amorphous.

The experimental annealing between 400 and 800 °C induced recrystallization to a phase with an X-ray powder diffraction pattern that corresponds to a cubic symmetry, namely the space group *Fm-3m*. Very similar results were obtained by Bulakh et al. (1998) after heating metamict "*zirkelite*" from Sebl'yavr, Kola Peninsula, Russia at 600–1000 °C. However, goniometric measurements and stereographic projections of their results confirmed a cubic symmetry and a space group *Fm3m* of their cubooctahedral specimens. Their minerals were thus interpreted to match the cubic zirkelite sensu stricto (Bayliss et al. 1989) at the time of their formation. By contrast, thorough examination of the morphology of the metamictized zirconolite crystals from the LPC by means of reflection goniometry (Brøgger 1890), as well as more recent examination of the habits of Stålaker zirconolite (Larsen 2010, see the figure on the page 222) revealed well developed long prismatic, pyramidal as well as basal pinacoidal faces corresponding to orthorhombic symmetry. Brøgger (1890) obtained an axial ratio *a:b:c* = 0.712 : 1 : 0.512, which is in very good agreement with the ratio 0.717 : 1 : 0.515 reported by Mazzi and Munno (1983) for crystalline zirconolite-*3O* from Campi Flegrei, Italy.

Nevertheless, metamict zirconolite from Sri Lanka initially recrystallized to a cubic, fluorite-type structure prior to a second phase transformation into highly twinned monoclinic structural type intergrown by other polytypes at higher temperature (Lumpkin et al. 1986). In a similar manner, synthetic, originally monoclinic, Cm-doped self-radiation damaged zirconolite heated at 575–850 °C and gave an X-ray diffraction pattern very similar to the pattern of our cubic phase (Fig. 1b), while further heating between 900 and 1150 °C restored original monoclinic symmetry (Weber et al. 1986). Regarding formation of the cubic phase in our experiment, we adopt suggestions of Lumpkin et al. (1986) and Weber et al. (1986) that amorphous zirconolite initially recrystallizes

to a disordered, defect fluorite structure. Obviously, the empirical observations together with disagreement between morphology of Norwegian zirconolite and XRPD patterns of the initial annealed phase clearly indicate that original structural type has not been recovered between 400 and 800 °C.

Rietveld analysis of the XRPD pattern acquired at 900 °C implies that the material recrystallized to a mixture of two polytypes – an orthorhombic predominating over the trigonal. Twinning of zirconolite and intergrowths of the different structural polytypes have been observed in both, synthetic (e.g. White 1984) as well as natural (e.g. Mazzi and Munno 1983; Bellatreccia et al. 2002; Zubkova et al. 2018) zirconolite. Difficulties with a structural description of zirconolite have been discussed by Bellatreccia et al. (2002) who described an acicular, non-metamict zirconolite from syenitic ejecta of the Vivo volcanic complex, Italy, interpreted as zirconolite-*3O* with electron diffraction pattern, however, showing many features consistent with -*3T* polytype. Zubkova et al. (2018) observed intergrowths of a crystalline zirconolite-*3T* and a morphologically different, acicular zirconolite-*3O* (stefanweissite according to Chukanov et al. 2019) occurring in cavities of a nosean syenite in the Laacher See volcano, Germany. The recrystallization of our studied material highly probably resulted in such kind of intergrowths of the two latter structural types.

Nevertheless, the thermal annealing experiment on metamict mineral does not prove the original crystal structure was restored (e.g., Tomašić et al. 2006; Britvin et al. 2019). Careful goniometric measurements of similar "*polymignyte*" crystals from the same region by Brøgger (1890) and examination of the habits of the Stålaker zirconolite (Larsen 2010), as described above, strongly suggests that our studied zirconolite originally crystallized as the orthorhombic polytype. Unlike

in the case of the intergrowths described from Laacher See, no morphological features characteristic for a trigonal symmetry has been observed.

Comparison of chemical compositions with other zirconolite occurrences

In contrast to the ideal zirconolite composition, our investigated zirconolite samples are strongly enriched in REE's, actinides, Fe as well as in Nb, which matches well with zirconolite-related minerals from Laacher See (Della Ventura et al. 2000; Chukanov et al. 2018, 2019; Zubkova et al. 2018). In both of the ternary plots comparing contents of components allocated into M[VIII] or M[VI,V,IV] sites, respectively, our compositions are scattered very close to type stefanweissite and nöggerathite (Fig. 9). The most significant difference regarding chemical compositions in our samples are the moderate manganese content of up to c. 0.8 wt% MnO, while zirconolite-related minerals from Laacher See have a high content of 2-9.4 wt% MnO. Despite the elevated actinide concentrations in zirconolite from the both regions, our samples are of Permian age and thus completely radiation-damaged (radiation doses $\geq 10^{16}$ α-decays/mg) unlike young Quaternary c. 13 ka old (e.g., Bogaard 1995) and fully crystalline minerals (doses of $\leq 2\times10^{12}$ α-decays/mg; our calculations from the published compositions) from Laacher See. Such young crystals are favorable for structure refinement by means of single-crystal X-ray diffraction, based on which Chukanov et al. (2014, 2018, 2019) reported ordering of Nb and Ti octahedral sites. Although our investigated metamict minerals should be labelled zirconolite (without a suffix) in accordance with Bayliss et al. (1989), their empirical formulae (as well as the assumed structure type) correspond well to type stefanweissite or nöggerathite (in the case of the four most REE-rich Stålaker compositions giving X_{REE} = 0.502–0.504, thus REE>Ca). We suggest that ordering of Ti and Nb could also occur in crystal structures of zirconolite crystals from Larvik

Plutonic Complex at the time of their formation. If so, zirconolite from Håkestad, Agnes and Stålaker are essentially identical minerals as the crystalline analogues of ziroconolite-*3O*, stefanwessite and/or nöggerathite, respectively from Laacher See.

Nevertheless, empirical formula of zirconolite-*3T* from Laacher See (Zubkova et al. 2018) is very similar to the formula of type stefanweissite as well as of zirconolite described in this study (compare the plotted compositions in Fig. 9). The occurrences of zirconolite-*3T* associated (and intergrown) with orthorhombic stefanweissite in Laacher See as well as assumed intergrowths of the both structural types in our thermally annealed material imply that both structural types may be formed having almost identical composition at identical P-T conditions.

In contrast to the tiny, up to several tens of micrometers long, crystals from Laacher See, zirconolite from Larvik Plutonic Complex occur as macroscopic crystals, several centimeters in length.

Apart from the above-mentioned reference specimens from Laacher See, zirconolite from Schryburt Lake, Canada (Gieré et al. 1998) are characterized by elevated contents of up to c. 21 wt% REE_2O_3 as well as up to c. 16 wt% Nb_2O_5, which are similar to our samples (Fig. 9).

With regard to the chondrite-normalized REE patterns, the preferential incorporation of light to medium rare earth elements observed in our compositions (Fig. 3) is relatively common. Well-pronounced patterns of this type were yielded by REE-rich zirconolite originating from sanidinite from Laacher See, Germany (Della Ventura et al. 2000, Chukanov et al. 2018, 2019) or carbonatites from Schryburt Lake, Canada or Araxá, Brazil (both reported by Williams and Gieré 1996 and Gieré et al. 1998; see also the bright reference REE pattern in Fig. 3). On the contrary, a different type of REE pattern with elevated contents of yttrium and heavy rare earth elements (dark reference REE pattern in Fig. 3) is given by a distinct kind of REE-rich zirconolite. This

group comprises samples from lunar basalt (Rasmussen et al. 2008), metasomatic fracture fillings from Koberg Mine, Sweden (Zakrzewski et al. 1992), a marble skarn from Bergell, Switzerland (Gieré 1986; Williams and Gieré 1988), a sapphirine granulite from Vestfold Hills, Antarctica (Harley 1994), a nepheline syenite from Tchivira, Angola (Williams and Gieré 1996), a gabbro pegmatite from St. Kilda, Scotland (Harding et al. 1982) and an alkaline metasomatite from Dmitrovka, Ukrainian Shield (Sharygin 2014).

Relationships among Håkestad-type mode, stefanweissite and nöggerathite within the composition space $(Ca,REE)_2Zr_2(Ti,Me^{5+})_3(Me^{2+})O_{14}$

We suggested above that our observed compositions as well as compositions of type stefanweissite (and nöggerathite) can be approximated by involvement of the intermediate endmember $CaREEZr_2Ti_2Me^{5+}Me^{2+}O_{14}$, which is supported by the projection of these compositions into ternary plots in Figs. 9 and 10. If such endmember is mixed with the ideal laachite formula, $Ca_2Zr_2Me^{5+}{}_2TiMe^{2+}O_{14}$, resultant compositions show predominance of Ca over REE and Nb may still prevail over Ti in only one octahedral site at a certain range of mixing ratios, thus agreeing with the definition of stefanweissite. It is noteworthy, that slight distortion of a crystal structure should occur between laachite and stefanweissite compositions. Although both minerals are analogs of zirconolite-*3O*, the former is monoclinic (pseudo-orthorhombic, β = 90.072°), while the latter is orthorhombic (Chukanov et al. 2014, 2019).

On the other hand, to get compositions with REE>Ca, the composition space must be extended towards Ca-free, REE-bearing terminal composition. Regarding a simplified subspace $(Ca,REE)Zr_2(Ti,Me^{5+})_3Me^{2+}O_{14}$, the only possibility is to lengthen the substitution vector REE + Ti = Ca + Nb from laachite via the intermediate CaREE-member towards $REE_2Zr_2Ti_3Me^{2+}O_{14}$ (Fig. 10). The higher Ti/Me^{5+} ratio observed in type nöggerathite compared to type stefanweissite

agrees with this substitution vector. Given that the compositions of ideal laachite (note that type laachite composition remarkably deviates from the ideal) and type stefanweissite and nöggerathite are approximately colinear in ternary plots in Figs. 9 and 10, the suggested colinear endmember series model nicely approximates the relationships among these 3 minerals.

In actuality, type (and co-type) nöggerathite compositions from Chukanov et al. (2018) defined as REE-dominant are rather close to the intermediate endmember, $CaREEZr_2Ti_2Me^{5+}Me^{2+}O_{14}$, and slightly differ from type stefanweissite (see their Fig. 6 and our Figs. 9, 10; The positions of the plotted points somewhat differ between their projections and ours). In their ternary plot, the cited authors neglected a significant fraction of Mn allocated into the M[VIII] site according to their structural model, while we added this fraction of Mn to divalent Ca. We suggest that instead of using the dominant constituent rule, the difference between type nöggerathite and stefanweissite could be more convincingly demonstrated using an extension of the dominant valency rule after Bosi et al. (2019). As the type nöggerathite is enriched in actinides, the root-charge arrangement $(M^{3+})_2Zr_2Ti_3Fe^{2+}O_{14}$ predominates over $(M^{2+})_2Zr_2Nb_2TiFe^{2+}O_{14}$ in the mineral if the CaACT configuration is considered (along with REE_2) to represent $(M^{3+})_2$ (see Bosi et al. 2019).

Obviously, compositions of the $Ca_2Zr_2Me^{5+}{}_2TiMe^{2+}O_{14}$ – $REE_2Zr_2Ti_3Me^{2+}O_{14}$ series approaching the latter endmember break the definition of "Nb prevailing in one octahedral site" despite being REE-dominant and thus can not be classified as nöggerathite. Although the zirconolite endmember $REE_2Zr_2Ti_3Me^{2+}O_{14}$ has not been described yet, similar, or related compositions have been published (Fig. 9). The closest of them is likely the composition of zirconolite from Dmitrovka metasomatite, Ukrainian Shield, reported by Sharygin (2014) and characterized by formula (after recalculation per 14 O): $Y_{1.4}HREE_{0.4}Ca_{0.2}Zr_2Ti_{2.6}Nb_{0.4}Mn_{0.6}Fe^{2+}{}_{0.4}O_{14}$, (actually with Mn>Fe). Existence of this previously unrecognized endmember is also strongly supported by compositions of lunar zirconolite described by Brown et al. (1972), Busche et al. (1972),

Roedder and Weiblen (1973), Wark et al. (1973), Meyer and Boctor (1974) and tabled by Williams and Gieré (1996) and those by Rasmussen et al. (2008), (Fig. 9). The fact that ferric iron was not detected in lunar rocks (e.g., Herzenberg and Riley 1970, Wadhwa 2008) indicates the REE-rich and Nb-poor compositions cannot be explained in terms of endmembers suggested by Gieré et al. (1998) as their only REE- and Ti- dominated endmember ($REE_2Zr_2Ti_2Me^{3+}{}_2O_{14}$) contains trivalent Fe. Further occurrences of zirconolite containing high amounts of the $REE_2Zr_2Ti_3Me^{2+}O_{14}$ endmember, as obvious from Fig. 9, are the nepheline syenite from Tchivira, Angola (Williams and Gieré 1996), the sapphirine granulite from Vestfold Hills, Antarctica (Harley 1994) and the gabbro pegmatite from St. Kilda, Scotland (Harding et al. 1982). It should be noted that these zirconolite samples are characterized by preferential incorporation of yttrium and heavy rare earth elements (Fig. 3). Unlike its Nb- (and possibly Ca-) enriched analogs, crystal-chemical configuration of $REE_2Zr_2Ti_3Me^{2+}O_{14}$ thus seems to be favorable for enrichment in heavy REE.

Relevance of an extended composition space $(Ca,REE,ACT)_2Zr_2(Ti,Me^{5+})_3(Me^{2+},Me^{3+})O_{14}$

Projections of our compositions from Håkestad and Agnes in the Ti– (Me^{2+} + Me^{3+})–Me^{5+} ternary plot (Fig. 9b) are nearly colinear with points representing endmember series $Ca_2Zr_2Me^{5+}{}_2TiMe^{2+}O_{14}$ – $REE_2Zr_2Ti_3Me^{2+}O_{14}$ mentioned earlier in the text. All of the compositions are plotted between $Me^{5+}{}_2Ti(Me^{2+},Me^{3+})$, and $Ti_3(Me^{2+},Me^{3+})$ line segments in Figs. 9, 10. In contrast to the mentioned model endmembers, our natural compositions show significant and somewhat variable contents of actinides and trivalent iron. As shown above, this compositional behavior can be simulated by coupling of the corresponding ACT- and Me^{3+}-bearing endmembers of Gieré et al. (1998) with ideal zirconolite. It provides clear evidence of involvement of ACT- and Me^{3+}- bearing analogs of the endmembers from the subspace

$(Ca,REE)_2Zr_2(Ti,Me^{5+})_3Me^{2+}O_{14}$. Such analogs could be characterized by the following chemical formulae (Fig. 10): $CaACTZr_2Ti_3Me^{2+}O_{14}$, $Ca_2Zr_2Ti_2Me^{5+}Me^{3+}O_{14}$, $CaREEZr_2Ti_3Me^{3+}O_{14}$. In fact, a large number of c. 450 published natural zirconolite compositions cluster around the $Me^{5+}{}_2Ti(Me^{2+},Me^{3+})$–$Ti_3(Me^{2+},Me^{3+})$ line segment in the Ti– $(Me^{2+}+Me^{3+})$–Me^{5+} ternary plot (Figs. 9, 10), implying that the modified endmember scheme could be compatible with many natural zirconolite compositions.

Iron oxidation state and its relationship to other composition variables

Our presented data yield a good agreement between the oxidation state of iron determined using Mössbauer spectroscopy and charge-balance-based calculations. It implies that the latter indirect quantification may give meaningful values.

Zirconolite from Schryburt Lake, Canada (Gieré et al. 1998) shows wide ranges of X_{REE} and X_{Me5+}, and relatively low actinide contents (Fig. 9a). In addition, like the compositions described above, compositions from Schryburt Lake cluster around the $Me^{5+}{}_2Ti(Me^{2+},Me^{3+})$–$Ti_3(Me^{2+},Me^{3+})$ line segment in the Ti–$(Me^{2+}+Me^{3+})$–Me^{5+} ternary plot (Fig. 9b). Such compositional behavior could be represented by a simplified, actinide-free composition subspace $(Ca,REE)_2Zr_2(Ti,Me^{5+})_3(Me^{2+},Me^{3+})O_{14}$ constrained by the endmember set from the two previous sections. Thus, there should be a clear relationship among the composition variables X_{REE}, X_{Me5+} and oxidation state of iron, X_{Fe3+}, or rather $X_{Me3+} = (Me^{3+})/(Me^{3+} + Me^{2+})$. In other words, X_{REE} and X_{Me5+} values should span a constrained field in a corresponding binary plot and provide an independent estimate of X_{Me3+} (although X_{Fe3+} and X_{Me3+} are mostly equal, they may differ in Mg-, Mn-, or Al-enriched compositions, respectively). The relationship is as follows:

$$X_{Me3+} = 2 - 2\,X_{REE} - 3\,X_{Me5+} \quad (1)$$

As seen in Fig. 9b, numerous compositions of zirconolite worldwide are shifted towards the vertex Ti (i.e. contain < 1 Me^{2+} + Me^{3+} atom per 14 O) compared to Schryburt Lake zirconolite. We assume that in most cases, this is due to the involvement of uncoupled ideal zirconolite in the solid solution. Moreover, Fig. 9a shows that a large number of REE-enriched compositions contain significant amounts of actinides. Therefore, participation of $CaACTZr_2Ti_3Me^{2+}O_{14}$ showing the same root-charge arrangement as $REE_2Zr_2Ti_3Me^{2+}O_{14}$ (and thus plotted in the same point in Fig. 11a) is considered. The improved calculation regarding participation of the two additional endmembers becomes (see Appendix C for details of the approach):

$$X_{Me3+} = 2 - 2X_{REE*} - 3X_{Me5+*} \quad (2)$$

where the modified variables (with asterisk) are defined as follows:

$$X_{REE*} = \frac{(REE+2ACT)}{[REE+ACT+Ca-2X_{id}]} \quad (3)$$

$$X_{Me^{5+}*} = \frac{Me^{5+}}{[Me^{5+}+Ti-4X_{id}]} \quad (4)$$

$$X_{id} = \frac{4(Ti+Me^{5+})}{(Me^{2+}+Me^{3+}+Me^{5+}+Ti)} - 3 \quad (5)$$

To test the suggested relationship, Eq. 2 was solved for zirconolite compositions from 7 occurrences worldwide (109 analyses), all of which contain approximately 1 atom Me^{2+} + Me^{3+} per 14 O. The results were compared with X_{Me3+} obtained from the charge-balanced stoichiometric formulae (based on 8 cations and 14 oxygens). The following zirconolite occurrences were used in this test: Schryburt Lake, Canada (Williams and Gieré 1996; Gieré et al. 1998), Kovdor, Russia (Williams 1996; Williams and Gieré 1996; Wu et al. 2010); Evate, Mozambique (Hurai et al. 2018); Vestfold Hills, Antarctica (Harley 1994); Tchivira, Angola (Williams and Gieré 1996); Koberg, Sweden (Zakrzewski et al. 1992; Williams and Gieré 1996); Malawi (Platt et al. 1987; Williams and Gieré 1996).

As demonstrated in Figure 11b, X_{Me3+} values determined from Eq. 2 agree well with the charge-balance-based X_{Me3+} values, even though both are indirect and mutually independent estimates rather than originating from instrumental measurements of iron oxidation state. It should be noted, that Gieré et al. (1998) assumed zirconolite from Schryburt Lake to be dominated by trivalent iron based on strong negative correlations between REE vs. Ca and between Ti vs. Me^{5+}. Regarding their set of endmembers, this could only be explained by substitution #22 (Ca + Me^{5+} = REE + Ti) between two ferric-iron-bearing endmembers, $Ca_2Zr_2Me^{5+}{}_2Me^{3+}{}_2O_{14}$ and $REE_2Zr_2Ti_2Me^{3+}{}_2O_{14}$ (see their Fig. 3). Nevertheless, our calculation shows that these compositions are plotted in the ferrous-iron-dominated part of the diagram in Fig. 11a, and may be expressed through participation of three major endmembers, e.g. $Ca_2Zr_2Me^{5+}{}_2TiMe^{2+}O_{14}$, $REE_2Zr_2Ti_3Me^{2+}O_{14}$ and $CaREEZr_2Ti_3Me^{3+}O_{14}$ marked with I., III., IV. in the plot (accompanied by small amounts of $CaACTZr_2Ti_3Me^{2+}O_{14}$ and uncoupled ideal zirconolite). The calculated X_{Me3+} values are in perfect agreement with X_{Me3+} obtained from charge-balanced formulae (Fig. 11a, b). Although our explanation validates the major role of substitution #22 (Ca + Nb = REE + Ti) as seen in Fig. 11a, we oppose the conclusion of Gieré et al. (1998) that this mechanism operates between two ferric iron-bearing endmembers as predominant constituents.

Relationship of X_{Fe3+} in zirconolite to redox conditions during crystallization

Our studied zirconolite yields moderate X_{Fe3+} values below c. 0.2. The redox conditions during the crystallization of larvikite in the host complex were buffered by silicate melt, Fe-Ti oxides and mafic silicates to approximately one log(f_{O2}) unit below the QFM (quartz – fayalite – magnetite) buffer (Neumann 1976). The associated zirconolite-bearing alkaline pegmatites are assumed to show comparable redox conditions (Andersen et al., 2013). Similar X_{Fe3+} values below c. 0.1 were given by stoichiometric, charge-balanced formulae of zirconolite from

chromites in the Finero Complex, Italy (Zaccarini et al., 2004), in which the mineral is genetically related to olivine – spinel symplectites giving log(f_{O2}) values between QFM-3.2 and QFM+1.8.

However, oxidation state of iron in zirconolite can vary from purely ferrous to purely ferric, as obvious from Figure 11. On the one hand, the former sort of zirconolite may crystallize in strongly reducing conditions such as lunar basalts, where iron occurs solely in metallic or divalent form (Herzenberg and Riley 1970, Wadhwa 2008). These extraterrestrial rocks show oxygen fugacity values equal or below the IW (iron – wüstite) buffer, i.e. c. 4 to 6 orders of magnitude below the QFM buffer (e.g. Wadhwa 2008 and references therein). By contrast, Carlier and Lorand (2008) reported ferric zirconolite (giving X_{Fe3+} values of c. 1 based on charge-balanced stoichiometric formulae) associated with hematite in groundmass. The host potassic kersantite in Oroscocha Quaternary Volcano, Peru, underwent drastic late-magmatic oxidation, during which log(f_{O2}) increased from QFM-1 to QFM+5, above the HM (hematite – magnetite) buffer. Furthermore, ferric-iron-dominated zirconolite was described by Hurai et al. (2018) from the Evate apatite deposit, Mozambique, where the oxidation event is assumed to correlate with infiltration of oxidizing, hematite-buffered, sulfate-rich brines, the remnants of which are preserved as fluid inclusions in apatite. Occurrences of zirconolite in such distinct geological environments imply that the mineral may crystallize in a very wide range of redox conditions.

Necessary extension of zirconolite composition space

The composition space as defined by Gieré et al. (1998) is insufficient to describe compositions outside the triangle outlined by points II., IV., and V. in the plot in Fig. 11a. Obviously, all published compositions of zirconolite from Kovdor, Kola Peninsula (Williams and Gieré 1996), compositions approaching laachite, $Ca_2Zr_2Me^{5+}{}_2TiMe^{2+}O_{14}$ (mark I.), or the new endmember

revealed in this study, $REE_2Zr_2Ti_3Me^{2+}O_{14}$ (mark III.), could not be projected in the original composition space. However, the set of 5 linearly independent endmembers from Gieré et al. (1998) is meaningful and satisfactory. The modified (and extended) reciprocal composition subspace (e.g., Dolivo-Dobrovol´sky 2010) suggested in this study can be described by linear combination of the members of this basic set, but subtraction, not considered by Gieré et al. (1998), must be involved in these operations. The following linear algebraic expressions demonstrate the relationship between the two sets of endmembers:

$$\begin{bmatrix} 1 & 0 & 0 & 0 & 0 & 0 \\ 0 & 1 & 0 & 0 & 0 & 0 \\ 0 & 0 & 1 & 0 & 0 & 0 \\ 0 & 0 & 0 & 1 & 0 & 0 \\ 0 & 0 & 0 & 0 & 1 & 0 \\ 0 & 0 & 0 & 0 & 0 & 1 \end{bmatrix} \cdot \begin{bmatrix} Ca_2Zr_2Me_2^{5+}TiMe^{2+}O_{14} \\ CaREEZr_2Ti_2Me^{5+}Me^{2+}O_{14} \\ REE_2Zr_2Ti_3Me^{2+}O_{14} \\ CaACTZr_2Ti_3Me^{2+}O_{14} \\ CaREEZr_2Ti_3Me^{3+}O_{14} \\ Ca_2Zr_2Ti_2Me^{5+}Me^{3+}O_{14} \end{bmatrix} = \begin{bmatrix} 0.5 & 0.5 & 0 & -0.5 & 0.5 \\ 0.5 & 0.5 & 0 & 0 & 0 \\ 0.5 & 0.5 & 0 & 0.5 & -0.5 \\ 0.5 & 0 & 0.5 & 0 & 0 \\ 0.5 & 0 & 0 & 0.5 & 0 \\ 0.5 & 0 & 0 & 0 & 0.5 \end{bmatrix} \cdot \begin{bmatrix} Ca_2Zr_2Ti_4O_{14} \\ REE_2Zr_2Me_2^{5+}Me_2^{2+}O_{14} \\ ACT_2Zr_2Ti_2Me_2^{2+}O_{14} \\ REE_2Zr_2Ti_2Me_2^{3+}O_{14} \\ Ca_2Zr_2Me_2^{5+}Me_2^{3+}O_{14} \end{bmatrix} \quad (6)$$

IMPLICATIONS

Natural zirconolite is an example of a complex mineral composed of a high number of chemical constituents (24 elements were detected by EPM analyses in our study) occupying several distinct crystallographic sites. The corresponding composition space may be simplified, and the number of chemical constituents reduced by grouping of elements based on their valences and affinities for the given crystallographic sites (e.g., Gieré et al. 1998). Despite this, the involvement of about 5 or more major endmembers in such a solid solution gives a set of about 10 or more basic substitution vectors to be regarded during a statistical analysis performed to describe the

substitutional behavior. However, participation of any of these vectors is inferred from an even higher number of binary (constituent-constituent pair) relationships (see e.g., correlation matrices in Tabs. A1 to A9 in Gieré et al. 1998). Moreover, identification of the basic vectors alone is insufficient for a quantitative description of a compositional behavior of a zoned mineral grain or a mineral population, respectively. Instead, the compositional variability may be, in many cases, unequivocally and simply characterized by a single, composite, general vector, which results from a linear combination of the several basic vectors. The mixing of several endmembers may be alternatively expressed as a binary mixing between two terminal (and hypothetical) compositions situated at the edges (i.e. where content of at least one constituent drops to zero) in the composition space as shown in the cases above. Thus, they are called *edgemembers* in our study. Unlike endmembers, the *edgemember* compositions are only meaningful for a distinct characteristic trend of a mineral population or a zoned mineral. Nevertheless, the general substitution vector may be very simply obtained from the difference between the pair of *edgemembers*. Therefore, identification of this pair provides a simple and fully quantitative description of the compositional behavior. Obviously, this concept is not restricted to the study of zirconolite and may be applied to other complex solid solutions.

Despite the remarkable compositional variability of natural zirconolite, the content of Zr is relatively regular and somewhat uncommonly deviates from c. 2 atoms per 14 O. Therefore, the set of zirconolite endmembers suggested in this study, like the endmember set of Gieré et al. (1998), does not consider Zr to enter sites other than M[VII] or be substituted by other elements in significant amounts, as a reasonable approximation. In addition, both approaches regard chemical composition and empirical allocation of the participating elements into nominally Ca- and Ti-bearing sites (Gieré et al. 1998), respectively, rather than detailed structural refinement (e.g., Chukanov et al. 2014, 2018, 2019). Such detailed structural data can hardly be refined for

most natural zirconolites. In particular, distribution of elements among the distinct octahedral, or split sites, all of which are nominally Ti-bearing, is highly uncertain, and thus not regarded.

In contrast to the composition space constrained by Gieré et al. (1998), the extended composition space suggested in our study comprises compositions approaching laachite, $Ca_2Zr_2Me^{5+}{}_2TiMe^{2+}O_{14}$ (Chukanov et al. 2014) and $REE_2Zr_2Ti_3Me^{2+}O_{14,}$ respectively. Obviously, the common substitution vector Ca + Nb = REE + Ti that is observed by Gieré et al. (1998), i.e. their vector #22, operates between these two endmembers (Figs. 9b, 10b, 11a). Therefore, this relationship does not necessarily indicate ferric-iron-bearing compositions (i.e. mixing of $Ca_2Zr_2Me^{5+}{}_2Me^{3+}{}_2O_{14}$ and $REE_2Zr_2Ti_2Me^{3+}{}_2O_{14}$), as the authors assumed (compare their interpretation of samples from Schryburt Lake, Kovdor and lunar basalts with our Figs. 9, 11). Furthermore, compositions of two analogs of zirconolite-*3O*: stefanweissite and nöggerathite agree with the scheme suggested in this study.

Based on these conclusions, we suggest a new scheme, comprising $Ca_2Zr_2Me^{5+}{}_2TiMe^{2+}O_{14}$ – $REE_2Zr_2Ti_3Me^{2+}O_{14}$ – $CaACTZr_2Ti_3Me^{2+}O_{14}$ – $CaREEZr_2Ti_3Me^{3+}O_{14}$ – $Ca_2Zr_2Ti_2Me^{5+}Me^{3+}O_{14}$ and ideal zirconolite, $Ca_2Zr_2Ti_4O_{14}$, to be well representative of zirconolite containing c. 2 atoms of Zr and Me^{2+} + Me^{3+} totaling ≤1 atom per 14 O, which is fulfilled by most natural zirconolite compositions (Figs. 9b, 10b). In addition, the suggested endmembers are closely approached by natural zirconolite compositions, unlike endmembers of Gieré et al. (1998), which are hypothetical and never closely approached by natural zirconolite. On the other hand, limited participation of the endmembers of Gieré et al. (1998) is observed in less common cases, in which the Me^{2+} + Me^{3+} sum exceeds unity (e.g. zirconolite from Stålaker described in this study). In such cases, endmembers from both sets may mix with each other but the ideal zirconolite formula is not involved.

The significance of the suggested scheme is strongly supported by the method successfully relating X_{Me3+} to other composition variables. As discussed above, the parameter X_{Me3+} is closely related to X_{Fe3+} and thus to iron oxidation state. In natural zirconolite, the X_{Fe3+} value may range between 0 and 1 and very likely reflects the redox conditions of the host environment during crystallization which may vary from strongly reducing to strongly oxidizing as shown above. We suggest that the new method of independent estimation of X_{Fe3+} as well as the improved knowledge of zirconolite mixing properties raise the potential of zirconolite as an indicator of redox conditions during crystallization of a host rock.

ACKNOWLEDGEMENTS

We wish to thank Gregory Lumpkin and Tonci Balic-Zunic for their constructive reviews on the manuscript and the associate editor Oliver Tschauner for his editorial work. The helpful assistance of Jordan Roberts with the English grammar is greatly appreciated.

REFERENCES CITED

Andersen, T., Erambert, M., Larsen, A.O., and Selbekk, R.S. (2010) Petrology of nepheline syenite pegmatites in the Oslo Rift, Norway: Zirconium silicate mineral assemblages as indicators of alkalinity and volatile fugacity in mildly agpaitic magma. Journal of Petrology, 51, 2303–2325.

Andersen, T., Erambert, M., Larsen, A.O., and Selbekk, R.S. (2013) Petrology of nepheline syenite pegmatites in the Oslo Rift, Norway: Zr and Ti mineral assemblages in miaskitic and agpaitic pegmatites in the Larvik Plutonic Complex. Mineralogia, 44, 61–98.

Bayliss, P., Mazzi, F., Munno, R., and White, T.J. (1989) Mineral nomenclature: Zirconolite. Mineralogical Magazine, 53, 565–569.

Bogaard, Pvd. (1995) $^{40}Ar/^{39}Ar$ ages of sanidine phenocrysts from Laacher See Tephra (12,900 yr BP): Chronostratigraphic and petrological significance. Earth and Planetary Science Letters, 133, 163–174.

Borodin, L.S., Nazarenko, I.I., and Richter, T.L. (1956) Zirconolite, a new mineral complex oxide AB_3O_7. Doklady Akademii Nauk SSSR, 110, 845–848 (in Russian).

Borodin, L.S., Bykova, A.V., Kapitonova, T.A., and Pyatenko, Y.A. (1960) New data on zirconolite and its niobium variety. Doklady Akademii Nauk SSSR, 134, 1022–1024 (in Russian).

Bosi, F., Hatert, F., Hålenius, U., Pasero, M., Miyawaki, R., and Mills, S.J. (2019) On the application of the IMA- CNMNC dominant-valency rule to complex mineral compositions. Mineralogical Magazine, 83, 627–632.

Britvin, S.N., Pekov, I.V., Krzhizhanovskaya, M.G., Agakhanov, A.A., Ternes, B., Schüller, W., and Chukanov, N.V (2019) Redefinition and crystal chemistry of samarskite-(Y), $YFe^{3+}Nb_2O_8$: cation-ordered niobate structurally related to layered double tungstates. Physics and Chemistry of Minerals, 46, 727–741.

Brøgger, W.C. (1890) Die Mineralien der Syenitpegmatitgänge der südnorwegischen Augit und Nephelinsyenite. Zeitschrift für Kristallographie, Speziellen Teil, 16, 1–663.

Brown, G.M., Emeleus, C.H., Holland, J.G., Peckett, A., and Phillips, R. (1972) Mineral-chemical variations in Apollo 14 and Apollo 15 basalts and granitic fractions. Proceedings of the 3rd Lunar Science Conference, p. 141–157.

Bulakh, A.G., Nesterov, A.R., Williams, C.T., and Anisimov, I.S. (1998) Zirkelite from the Sebl'yavr carbonatite complex, Kola Peninsula, Russia: an X-ray and electron microprobe study of a partially metamict mineral. Mineralogical Magazine, 62, 837–846.

Bulakh, A.G., Nesterov, A.R., Anastasenko, G.F., and Anisimov, I.S. (1999) Crystal morphology and intergrowths of calzirtite $Ca_2Zr_5Ti_2O_{16}$, zirkelite $(Ti,Ca,Zr)O_{2-x}$, zirconolite $CaZrTi_2O_7$ in phoscorites and carbonatites of the Kola Peninsula (Russia). Neues Jahrbuch Für Mineralogie, Monatshefte, 1, 11–20.

Busche, F.D., Prinz, M., Keil, K., and Kurat, G. (1972) Lunar zirkelite: A uranium-bearing phase. Earth and Planetary Science Letters, 14, 313–321.

Carlier, G., and Lorand, J.P. (2008) Zr-rich accessory minerals (titanite, perrierite, zirconolite, baddeleyite) record strong oxidation associated with magma mixing in the south Peruvian potassic province. Lithos, 104, 54–70.

Chukanov, N.V, Krivovichev, S.V, Pakhomova, A.S., Pekov, I.V, Schäfer, C., Vigasina, M.F., and Van, K. V. (2014) Laachite, $(Ca,Mn)_2Zr_2Nb_2TiFeO_{14}$, a new zirconolite-related mineral from the Eifel volcanic region, Germany. European Journal of Mineralogy, 26, 103–111.

Chukanov, N.V, Zubkova, N.V, Britvin, S.N., Pekov, I.V, Vigasina, M.F., Schäfer, C., Ternes, B., Schüller, W., Polekhovsky, Y.S., Ermolaeva, V.N., and others (2018) Nöggerathite-(Ce), $(Ce,Ca)_2Zr_2(Nb,Ti)(Ti,Nb)_2Fe^{2+}O_{14}$, a new zirconolite-related mineral from the Eifel volcanic region, Germany. Minerals, 8, 449.

Chukanov, N.V, Zubkova, N.V, Pekov, I.V, Vigasina, M.F., Polekhovsky, Y.S., Ternes, B., Schüller, W., Britvin, S.N., and Pushcharovsky, D.Y. (2019) Stefanweissite, $(Ca,REE)_2Zr_2(Nb,Ti)(Ti,Nb)_2Fe^{2+}O_{14}$, a new zirconolite-related mineral from the Eifel paleovolcanic region, Germany. Mineralogical Magazine, 83, 607–614.

Clinard, F.W. Jr., Foltyn, E.M., and Ewing, R.C. (1991) Stored energy in natural zirconolite and its synthetic counterpart after alpha recoil self-irradiation damage. Journal of Nuclear Materials, 185, 202–207.

Čopjaková, R., and Houzar, S. (2009) Zirconolite in marble from Krahulov and age of HT/LP metamorphism in the contact aureole of the Třebíč pluton. Acta Musei Moraviae, Scientiae geologicae, 94, 67–76 (in Czech).

Čopjaková, R., Vrána, S., Houzar, S., Červený, A., and Malec, J. (2008) Zirconolite, baddeleyite and geikielite in clinohumite-spinel-forsterite marbles near Horažďovice and Prachatice in southwestern Bohemia. Acta Musei Moraviae, Scientiae geologicae, 93, 37–51 (in Czech).

Dahlgren, S. (2010): The Larvik Plutonic Complex: The larvikite and nepheline syenite plutons and their pegmatites. In A.O. Larsen, Ed., The Langesundsfjord. History, Geology, Pegmatites, Minerals, p. 26–37. Bode Verlag, Salzhemmendorf, Germany.

Dahlgren, S., Corfu, F., and Heaman, L.M. (1996) U-Pb time constraints, and Hf and Pb source characteristics of the Larvik plutonic complex, Oslo Paleorift. Geodynamic and geochemical implications for the rift evolution. In V.M. Goldschmidt Conference, Journal of Conference Abstracts, p.120, Heidelberg, Germany.

Della Ventura, G., Bellatreccia, F., and Williams, C.T. (2000) Zirconolite with significant REEZrNb(Mn,Fe)O_7 from a xenolith of the Laacher See eruptive center, Eifel volcanic region, Germany. The Canadian Mineralogist, 38, 57–65.

Dolivo-Dobrovol'sky, V.V (2010) Dominant valency, end members, and reciprocal systems. Geology of Ore Deposits, 52, 618–623.

Gatehouse, B., Grey, I., Hill, R., and Rossell, H. (1981) Zirconolite, $CaZr_xTi_{3-x}O_7$; Structure refinements for near-end-member compositions with x = 0.85 and 1.30. Acta Crystallographica, B37, 306–312.

Gieré, R. (1986) Zirconolite, allanite and hoegbomite in a marble skarn from the Bergell contact aureole: implications for mobility of Ti, Zr and REE. Contributions to Mineralogy and Petrology, 93, 459–470.

Gieré, R., and Williams, C.T. (1992) REE-bearing minerals in a Ti-rich vein from the Adamello contact aureole (Italy). Contributions to Mineralogy and Petrology, 112, 83–100.

Gieré, R., Williams, C.T., and Lumpkin, G.R. (1998) Chemical characteristics of natural zirconolite. Schweizerische Mineralogische und Petrographische Mitteilungen, 78, 433–459.

Grey, I.E., Mumme, W.G., Ness, T.J., Roth, R.S., and Smith, K.L. (2003) Structural relations between weberite and zirconolite polytypes—refinements of doped *3T* and *4M* $Ca_2Ta_2O_7$ and *3T* $CaZrTi_2O_7$. Journal of Solid State Chemistry, 174, 285–295.

Harding, R.R., Merriman, R.J., and Nancarrow, P.H.A. (1982) A note on the occurrence of chevkinite, allanite, and zirkelite on St. Kilda, Scotland. Mineralogical Magazine, 46, 445–448.

Harley, S.L. (1994) Mg-Al yttrian zirconolite in a partially melted sapphirine granulite, Vestfold Hills, East Antarctica. Mineralogical Magazine, 58, 259–269.

Hawthorne, F.C. (2002) The use of end-member charge-arrangements in defining new mineral species and heterovalent substitutions in complex minerals. The Canadian Mineralogist, 40, 699–710.

Herzenberg, C.L., and Riley, D.L. (1970) Mössbauer spectrometry of lunar samples. Science, 167, 683–686.

Holland, H.D., and Gottfried, D. (1955) The effect of nuclear radiation on the structure of zircon. Acta Crystallographica, 8, 291–300.

Hurai, V., Huraiová, M., Gajdošová, M., Konečný, P., Slobodník, M., and Siegfried, P.R. (2018) Compositional variations of zirconolite from the Evate apatite deposit (Mozambique) as an indicator of magmatic-hydrothermal conditions during post-orogenic collapse of Gondwana. Mineralogy and Petrology, 112, 279–296.

Keller, J. (1984) Der jungtertiäre Vulkanismus Südwestdeutschlands: Exkursionen im Kaiserstuhl und Hegau. Fortschritte der Mineralogie. Beiheft, 62, 2–35 (in German).

Larsen, B.T., Olaussen, S., Sundvoll, B., and Heeremans, M. (2008) The Permo-Carboniferous Oslo Rift through six stages and 65 million years. Episodes, 31, 52–58.

Larsen, A.O. (2010) The Langesundfjord. History, Geology, Pegmatites, Minerals. Bode Verlag, Salzhemmendorf, Germany.

Lorand, J.P., and Cottin, J.Y. (1987) A new natural occurrence of zirconolite ($CaZrTi_2O_7$) and baddeleyite (ZrO_2) in basic cumulates: The Laouni layered intrusion (southern Hoggar, Algeria). Mineralogical Magazine, 51, 671–676.

Lumpkin, G.R., Ewing, R.C., Chakoumakos, B.C., Greegor, R.B., Lytle, F.W., Foltyn, E.M., Clinard, F.W., Boatner, L.A., and Abraham, M.M. (1986) Alpha-recoil damage in zirconolite ($CaZrTi_2O_7$). Journal of Materials Research, 1, 564–576.

Lumpkin, G.R., Smith, K.L., and Gieré, R. (1997) Application of analytical electron microscopy to the study of radiation damage in the complex oxide mineral zirconolite. Micron, 28, 57–68.

Lumpkin, G.R., Smith, K.L., Blackford, M.G., Gieré, R., Williams, C.T. (1998): The crystalline-amorphous transformation in natural zirconolite: Evidence for long-term annealing. Material Research Society Symposium Proceedings, 506, 215–222.

Mazzi, F., and Munno, R. (1983) Calciobetafite (new mineral of the pyrochlore group) and related minerals from Campi Flegrei, Italy; Crystal structures of polymignyte and zirkelite; Comparison with pyrochlore and zirconolite. American Mineralogist, 68, 262–276.

McDonough, W.F., and Sun, S.S. (1995) The composition of the Earth. Chemical Geology, 120, 223–253.

Merlet, C. (1994) An accurate computer correction program for quantitative electron probe microanalysis. Microchimica Acta, 114, 363–376.

Meyer, H.O.A, and Boctor, N.Z. (1974) Opaque mineralogy: Apollo 17, rock 75035. In W.A. Gose, Ed., Proceedings of the Fifth Lunar Science Conference, p. 707–716. Lunar and Planetary Institute, Houston.

Neumann, E. R. (1976) Compositional relations among pyroxenes, amphiboles and other mafic phases in the Oslo Region plutonic rocks. Lithos, 9, 85-109.

Neumann, E.R. (1980) Petrogenesis of the Oslo Region larvikites and associated rocks. Journal of Petrology, 21, 499–531.

Petersen, J.S. (1978) Structure of the larvikite-lardalite complex, Oslo-region, Norway, and its evolution. Geologische Rundschau, 67, 330–342.

Petříček, V., Dušek, M., and Palatinus, L. (2014) Crystallographic computing system JANA2006: general features. Zeitschrift für Kristallographie. Crystalline Materials, 229, 345–352.

Piilonen, P.C., McDonald, A.M., Poirier, G., Rowe, R., and Larsen, A.O. (2012) The mineralogy and crystal chemistry of alkaline pegmatites in the Larvik Plutonic Complex, Oslo rift valley, Norway. Part 1. Magmatic and secondary zircon: Implications for petrogenesis from trace-element geochemistry. Mineralogical Magazine, 76, 649–672.

Piilonen, P.C., McDonald, A.M., Poirier, G., Rowe, R., and Larsen, A.O. (2013) Mafic minerals of the alkaline pegmatites in the Larvik Plutonic Complex, Oslo rift, Southern Norway. The Canadian Mineralogist, 51, 735–770.

Platt, R.G., Wall, F., Williams, C.T., and Woolley, A.R. (1987) Zirconolite, chevkinite and other rare earth minerals from nepheline syenites and peralkaline granites and syenites of the Chilwa Alkaline Province, Malawi. Mineralogical Magazine, 51, 253–263.

Rajesh, V.J., Yokoyama, K., Santosh, M., Arai, S., Oh, C.W., and Kim, S.W. (2006) Zirconolite and baddeleyite in an ultramafic suite from southern India: Early Ordovician carbonatite-type

melts associated with extensional collapse of the Gondwana crust. The Journal of Geology, 114, 171–188.

Rämö, O.T., and Andersen, T. (2011) Magmatic evolution of the Permo-Carboniferous Oslo rift: U-Pb- and Lu-Hf-in-zircon evidence from the 299–289 Ma Larvik plutonic complex. American Geophysical Union Fall Meeting, Abstract, V12B-02, San Francisco, USA.

Rasmussen, E., Neumann, E.R., Andersen, T., Sundvoll, B., Fjerdingstad, V., and Stabel, A. (1988) Petrogenetic processes associated with intermediate and silicic magmatism in the Oslo rift, south-east Norway. Mineralogical Magazine, 52, 293–307.

Rasmussen, B., Fletcher, I.R., and Muhling, J.R. (2008) Pb/Pb geochronology, petrography and chemistry of Zr-rich accessory minerals (zirconolite, tranquillityite and baddeleyite) in mare basalt 10047. Geochimica et Cosmochimica Acta, 72, 5799–5818.

Rickwood, P.C. (1968) On recasting analyses of garnet into end-member molecules. Contributions to Mineralogy and Petrology, 18, 175–198.

Roedder, E., and Weiblen, P.W. (1973) Petrology of some lithic fragments from Luna 20. Geochimica et Cosmochimica Acta, 37, 1031–1052.

Rossell, H.J. (1980) Zirconolite – A fluorite-related superstructure. Nature, 283, 282–283.

Sharygin, V.V. (2014) Y-REE-dominant zirconolite-group mineral from Dmitrovka metasomatites, Azov Sea region, Ukrainian shield. In N. Ilbeyli and M.G. Yalcin, Eds., 30th Internatinal Conference on “Ore Potential of Alkaline, Kimberlite and Carbonatite Magmatism”, Abstracts book, p. 156–158. Antalya, Turkey.

Sinclair, W., and Eggleton, R.A. (1982) Structure refinement of zirkelite from Kaiserstuhl, West Germany. American Mineralogist, 67, 615–620.

Sunde, Ø., Friis, H., and Andersen, T. (2018) Variation in major and trace elements of primary wöhlerite as an indicator of the origin of pegmatites in the Larvik plutonic complex, Norway. The Canadian Mineralogist, 56, 529–542.

Sunde, Ø., Friis, H., and Andersen, T. (2019) Pegmatites of the Larvik Plutonic Complex, Oslo Rift, Norway: Field relations and characterisation. Norwegian Journal of Geology, 99, 1–20.

Tomašić, N., Gajović, A., Bermanec, V., Su, D.S., Linarić, M.R., Ntaflos, T., and Schlögl, R. (2006) Recrystallization mechanisms of fergusonite from metamict mineral precursors. Physics and Chemistry of Minerals, 33, 145–159.

Wadhwa, M. (2008) Redox conditions on small bodies, the Moon and Mars. Reviews in Mineralogy and Geochemistry, 68, 493–510.

Wark, D.A, Reid, A.F., Lovering, J.F., and El Goresy, A. (1973) Zirconolite (versus zirkelite) in lunar rocks. Abstracts of the Lunar and Planetary Science Conference, 4, 764–766 (abstract).

Weber, W.J., Wald, J.W., and Matzke, H. (1986) Effects of self-radiation damage in Cm-doped $Gd_2Ti_2O_7$ and $CaZrTi_2O_7$. Journal of Nuclear Materials, 138, 196–209.

White, T.J. (1984) The microstructure and microchemistry of synthetic zirconolite, zirkelite and related phases. American Mineralogist, 69, 1156–1172.

Whittle K.R., Hyatt, N.C., Smith, K.L., Margiolaki, I, Berry, F.J., Knight, K.S., and Lumpkin, G.R. (2012) Combined neutron and X-ray diffraction determination of disorder in doped zirconolite-2M. American Mineralogist, 97, 291–298.

Williams, C.T. (1996) The occurrence of niobian zirconolite, pyrochlore and baddeleyite in the Kovdor carbonatite complex, Kola Peninsula, Russia. Mineralogical Magazine, 60, 639–646.

Williams, C.T., and Gieré, R. (1988) Metasomatic zonation of REE in zirconolite from a marble skarn at the Bergell contact aureole (Switzerland/Italy). Schweizerische Mineralogische und Petrographische Mitteilungen, 68, 133–140.

Williams, C.T., and Gieré, R. (1996) Zirconolite: A review of localities worldwide, and a compilation of its chemical compositions. Bulletin of the Natural History Museum London, 52, 1–24.

Wu, F.Y., Yang, Y.H., Mitchell, R.H., Bellatreccia, F., Li, Q.L., and Zhao, Z.F. (2010) In situ U-Pb and Nd-Hf-(Sr) isotopic investigations of zirconolite and calzirtite. Chemical Geology, 277, 178–195.

Wyckoff, R.W.G. (1963) Crystal structures, 467 p. Interscience Publishers, New York.

Zaccarini, F., Stumpfl, E. F., and Garuti, G. (2004) Zirconolite and Zr–Th–U minerals in chromitites of the Finero complex, Western Alps, Italy: evidence for carbonatite-type metasomatism in a subcontinental mantle plume. The Canadian Mineralogist, 42, 1825–1845.

Zakrzewski, M.A., Lustenhouwer, W.J., Nugteren, H.J., and Williams, C.T. (1992) Rare-earth minerals yttrian zirconolite and allanite-(Ce)* and associated minerals from Koberg mine, Bergslagen, Sweden. Mineralogical Magazine, 56, 27–35.

Zubkova, N. V., Chukanov, N. V., Pekov, I. V., Ternes, B., Schüller, W., Ksenofontov, D.A., and Pushcharovsky, D.Y. (2018) The crystal structure of nonmetamict Nb-rich zirconolite-3T from the Eifel paleovolcanic region, Germany. Zeitschrift für Kristallographie-Crystalline Materials, 233, 463–468.

LIST OF FIGURE CAPTIONS

Figure 1. X-ray powder diffraction patterns of thermally annealed zirconolite from the LPC and Rietveld refinement of the data. (a) Pattern of zirconolite annealed at 800 °C. Rietveld refinement is based on a structural model of a cubic ZrO_2 (labeled cub; Wyckoff 1963). (b) Pattern of zirconolite annealed at 900 °C. Rietveld refinement is based on structural models of

stefanweissite (labeled 3O; Chukanov et al. 2019) and zirconolite-*3T* (labeled 3T; Zubkova et al. 2018). Weight fractions of 0.612(4) and 0.388(5) are obtained for the two phases.

Figure 2. BSE images of zirconolite from the LPC. (a) Zirconolite from the Håkestad quarry. Simple magmatic zoning (if it occurs) may be visible in the BSE image. (b) Zirconolite from Agnes. Significant patchy zoning reflects contents of Th and U (higher contents in brighter zones).

Figure 3. Chondrite-normalized REE pattern of zirconolite from the LPC. Chondrite composition was adopted from McDonough and Sun (1995). The reference pattern of LREE-rich zirconolite was compiled with data from Williams and Gieré (1996) and that of HREE-enriched zirconolite was compiled with data from Williams and Gieré (1988), Harley (1994) and Rasmussen et al. (2008). See text for detailed description.

Figure 4. Diagrams showing compositional trends observed in zirconolite from the LPC. (a) Plot showing negative correlation between Ti and Nb. (b) Plot showing relationships among compositional variables X_{REE}, X_{Me5+} and actinide content. See text for explanation of the variables.

Figure 5. Ternary plots depicting chemical composition of zirconolite from the LPC. (a) Ca – ACT – REE plot involving elements assumed to occupy M[VIII] site. The relationship of compositional variable X_{Me5+} to these components is demonstrated using a color scale. (b) Ti – (Me^{2+} + Me^{3+}) – Me^{5+} plot involving elements assumed to occupy the M[VI,V,IV] sites. The relationship of ACT content to these components is demonstrated using a color scale.

Figure 6. Diagrams showing the compositional trends as a function of increasing ACT content. The compositional behavior is simulated by introduction of so called "*edgemembers*" (triangles). The dashed lines correspond to general vectors determined from the observed trends. See text for description of the approach.

Figure 7. Simulation of the observed data from Figs. 4b, 5 is based on 2-component mixing of two *edgemembers* (Fig. 6). *Edgemembers A* of both observed modes are close to endmember series $Ca_2Zr_2Me^{5+}{}_2TiMe^{2+}O_{14}$ – $CaREEZr_2Ti_2Me^{5+}Me^{2+}O_{14}$ – $REE_2Zr_2Ti_3Me^{2+}O_{14}$ (projected as filled circles in c). See text for description of the approach.

Figure 8. Quantitative model of involved endmember fractions (y axis) as a function of mixing ratio of *edgemember B* (primary x axis) or ACT content (secondary x axis). (a) Håkestad-type compositional trend. Note the coupling of linearly independent endmembers from the set by Gieré et al. (1998) (blue, green and yellow fields) providing a constant ratio of $(Me^{2+}+Me^{3+})/(Me^{2+}+Me^{3+}+Ti+Me^{5+})$ = 0.25. Alternatively, the set of linearly dependent endmembers (patterns) may be involved to describe such behavior. (b) Stålaker-type compositional trend. Note lack of the coupling in this mode.

Figure 9. Compositions of zirconolite from the LPC projected in the ternary plots involving elements assumed to occupy the M[VIII] (a) and M[VI,V,IV] (b) sites, respectively, and their comparison with other occurrences worldwide. The Ca vertex represents Ca + $^{[VIII]}$Mn in the cases of laachite, stefanweissite, nöggerathite and zirconolite-*3T* from Laacher See considering structural models of Chukanov et al. (2014, 2018, 2019) and Zubkova et al. (2018).

Figure 10. The linearly dependent endmembers suggested in this study (black filled circles, labels in bold) projected in the ternary plots involving elements assumed to occupy the M[VIII] (a) and M[VI,V,IV] (b) sites, respectively. About 450 published zirconolite compositions worldwide are projected for comparison (gray filled circles). Projections of the endmembers from the set by Gieré et al. (1998) are also shown (open circles, labels in plain).

Figure 11. (a) A diagram showing the relationships among the compositional variables X_{REE*}, X_{Me5+*} and X_{Me3+} (color scale) for zirconolite from 7 localities worldwide (109 analyses) showing $(Me^{2+} + Me^{3+})/(Me^{2+} + Me^{3+} + Ti + Me^{5+}) \approx 0.25$. The color of every point corresponds to charge-

balance-based X_{Me3+}, while the color isopleths are calculated from Eq. 2. (b) A diagram comparing the X_{Me3+} values obtained from the charge-balanced stoichiometric zirconolite formulae and X_{Me3+} calculated from Eq. 2, respectively. The same compositions as shown in (a) are plotted. Coefficient of determination: $R^2 = 0.9$.

Table 1. Representative electron microprobe analyses (wt%) and formulae of zirconolite from LPC.

Anal. num.	Håkestad 29./3	Håkestad 15/2.	Håkestad 21/2.	Agnes 39./3	Agnes 32./3	Agnes 37./3	Stålaker 1./3.	Stålaker 10./3	Stålaker 7./3.
Nb_2O_5	17.25	13.71	12.47	15.11	12.87	11.33	15.46	15.26	14.48
Ta_2O_5	1.04	1.10	1.06	0.81	0.84	1.02	0.86	0.98	1.23
SiO_2	0.00	0.00	0.00	0.09	0.08	0.11	0.13	0.10	0.07
TiO_2	17.43	20.14	20.87	18.59	20.77	20.56	17.29	17.48	17.34
ZrO_2	27.37	28.05	28.15	27.81	27.95	28.01	27.36	27.01	27.13
HfO_2	0.40	0.24	0.23	0.58	0.42	0.40	0.47	0.48	0.43
ThO_2	2.55	4.32	4.84	3.09	3.94	5.20	2.91	3.16	3.47
UO_2	0.65	1.39	1.79	1.38	1.62	2.46	0.81	0.97	1.36
Y_2O_3	1.44	1.39	1.45	1.38	1.55	1.80	1.96	1.97	2.14
La_2O_3	1.60	1.14	1.03	1.85	1.28	0.94	1.94	1.73	1.47
Ce_2O_3	6.57	5.05	4.37	5.38	5.28	4.76	7.25	7.13	6.59
Pr_2O_3	0.60	0.69	0.64	0.66	0.70	0.74	0.95	0.87	1.00
Nd_2O_3	2.17	2.81	2.86	2.11	2.61	2.96	2.83	2.92	3.58
Sm_2O_3	0.37	0.51	0.59	0.40	0.54	0.60	0.48	0.49	0.65
Gd_2O_3	0.32	0.33	0.45	0.28	0.39	0.46	0.37	0.47	0.45
Dy_2O_3	0.24	0.29	0.37	0.16	0.24	0.35	0.36	0.26	0.44
Er_2O_3	0.14	0.18	0.19	0.13	0.16	0.20	0.21	0.18	0.25
Yb_2O_3	0.13	0.18	0.22	0.25	0.20	0.05	0.15	0.23	0.23
MgO	0.06	0.16	0.15	0.07	0.12	0.21	0.14	0.16	0.20
CaO	7.60	7.25	7.11	7.85	7.23	6.53	6.60	6.31	5.90
MnO	0.88	0.66	0.61	0.72	0.61	0.54	0.64	0.68	0.64
FeO*	8.32	8.43	8.49	8.17	8.16	8.15	8.78	8.66	8.85
PbO	0.11	0.17	0.22	0.15	0.18	0.18	0.14	0.16	0.17
Total	97.24	98.19	98.16	97.02	97.74	97.56	98.09	97.66	98.07
REE_2O_3	*13.58*	*12.57*	*12.17*	*12.60*	*12.95*	*12.86*	*16.50*	*16.25*	*16.80*
Formulae on the basis of 8 cations and 14 oxygens									
Th	0.082	0.138	0.154	0.100	0.126	0.168	0.094	0.104	0.114
U	0.020	0.044	0.056	0.044	0.050	0.078	0.026	0.030	0.044
Y	0.108	0.104	0.108	0.104	0.116	0.136	0.148	0.150	0.164
La	0.084	0.058	0.054	0.096	0.066	0.050	0.102	0.092	0.078
Ce	0.340	0.258	0.224	0.278	0.272	0.248	0.378	0.374	0.348
Pr	0.030	0.036	0.032	0.034	0.036	0.038	0.050	0.046	0.052
Sm	0.018	0.024	0.028	0.020	0.026	0.030	0.024	0.024	0.032
Nd	0.110	0.140	0.144	0.106	0.130	0.150	0.144	0.150	0.184
Gd	0.016	0.016	0.020	0.014	0.018	0.022	0.018	0.022	0.022
Dy	0.010	0.014	0.016	0.008	0.010	0.016	0.016	0.012	0.020
Er	0.006	0.008	0.008	0.006	0.008	0.008	0.010	0.008	0.012
Yb	0.006	0.008	0.010	0.010	0.008	0.002	0.006	0.010	0.010
Ca	1.154	1.088	1.068	1.188	1.088	0.998	1.008	0.970	0.912
Pb	0.004	0.006	0.008	0.006	0.006	0.006	0.006	0.006	0.006
ΣM[VIII]	1.988	1.942	1.930	2.014	1.960	1.950	2.030	1.998	1.998
ACT	*0.106*	*0.188*	*0.218*	*0.150*	*0.182*	*0.252*	*0.126*	*0.140*	*0.164*
REE	*0.728*	*0.666*	*0.644*	*0.676*	*0.690*	*0.700*	*0.896*	*0.888*	*0.922*
Zr	1.890	1.916	1.926	1.916	1.914	1.950	1.900	1.892	1.908
Hf	0.016	0.010	0.010	0.024	0.016	0.016	0.020	0.020	0.018
Mn	0.106	0.078	0.072	0.086	0.072	0.066	0.078	0.082	0.078
ΣM[VII]	2.012	2.004	2.008	2.026	2.002	2.032	1.998	1.994	2.004
Nb	1.104	0.868	0.790	0.964	0.816	0.732	0.996	0.990	0.944
Ta	0.040	0.042	0.040	0.032	0.032	0.040	0.034	0.038	0.048
Si	0.000	0.000	0.000	0.012	0.012	0.016	0.018	0.014	0.010
Ti	1.856	2.122	2.202	1.974	2.194	2.208	1.852	1.888	1.882
Fe^{3+}	0.106	0.146	0.168	0.200	0.142	0.110	0.198	0.128	0.148
Mg	0.012	0.034	0.032	0.014	0.026	0.044	0.030	0.034	0.044
Fe^{2+}	0.878	0.842	0.828	0.766	0.816	0.864	0.848	0.912	0.920
ΣM[VI,V,IV]	3.996	4.054	4.060	3.962	4.038	4.014	3.976	4.004	3.996
Fe_{tot}	*0.984*	*0.988*	*0.996*	*0.966*	*0.958*	*0.974*	*1.046*	*1.040*	*1.068*
O^{2-}	14.000	14.000	14.000	14.000	14.000	14.000	14.000	14.000	14.000
Σcations	8.000	8.000	8.000	8.000	8.000	8.000	8.000	8.000	8.000

Note: FeO* represents hypothetical FeO equivalent to measured Fe

Figure 1

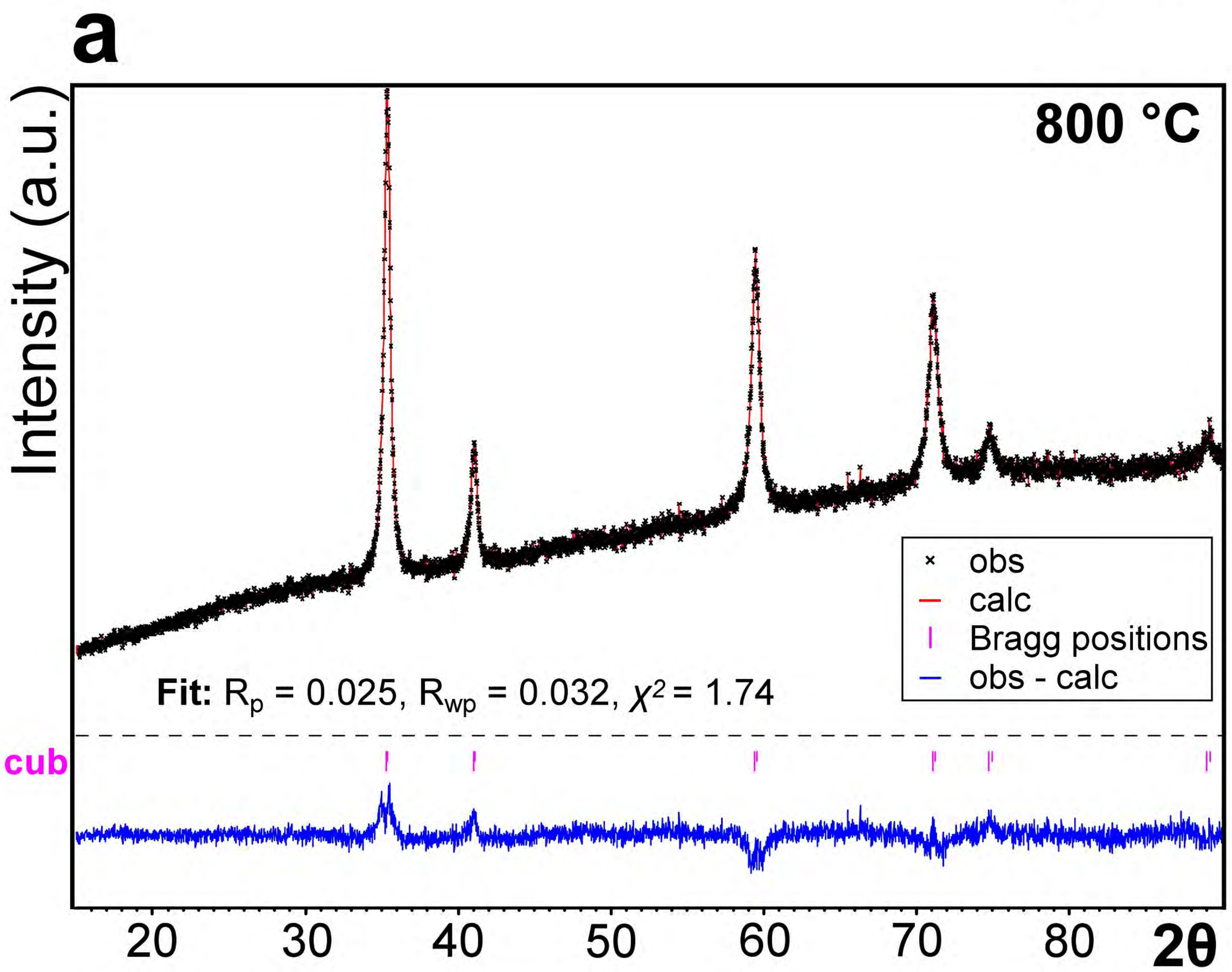
a
800 °C
Intensity (a.u.)
obs
calc
Bragg positions
obs - calc
Fit: R_p = 0.025, R_{wp} = 0.032, χ^2 = 1.74
cub
20
30
40
50
60
70
80
2θ

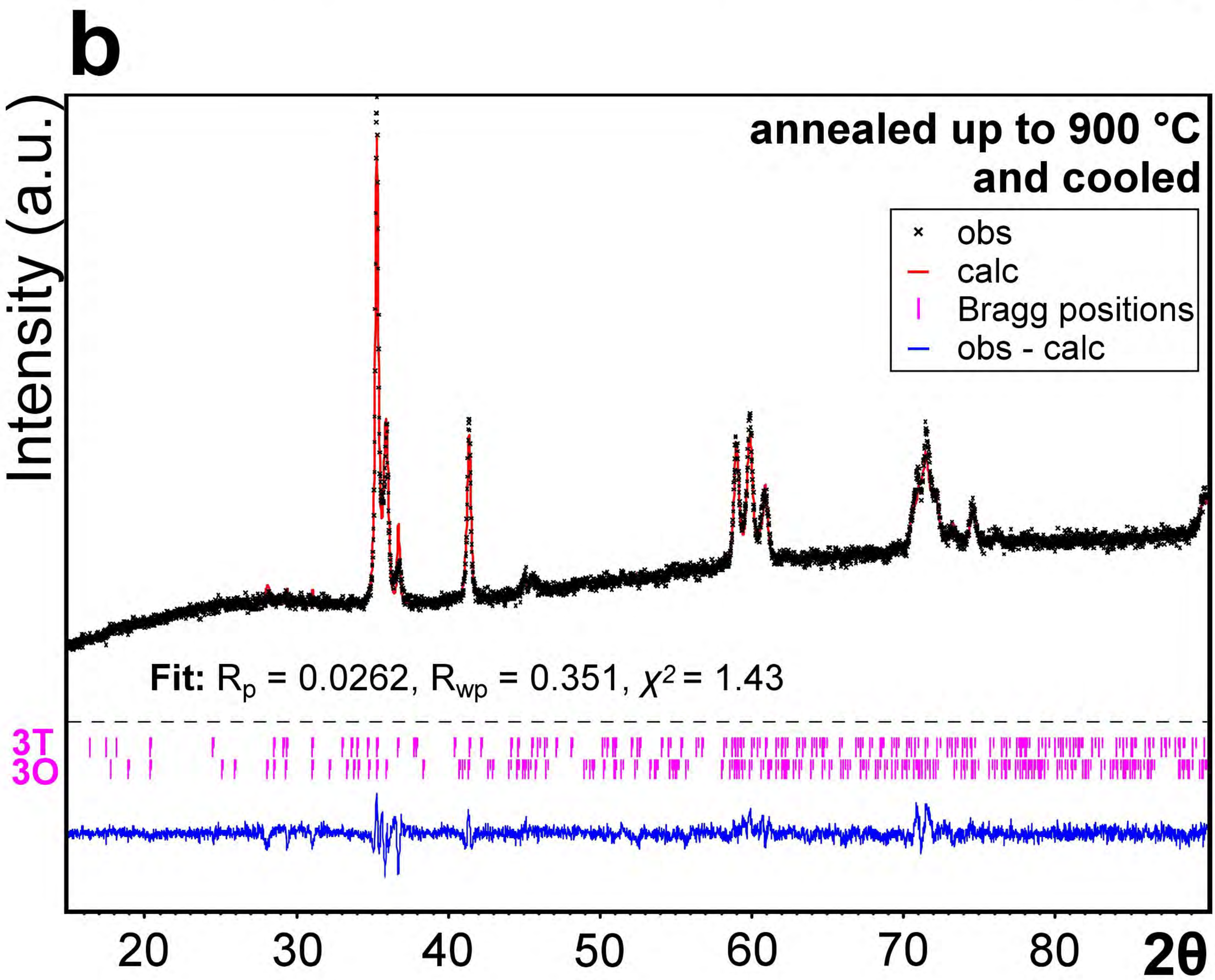
b
annealed up to 900 °C
and cooled
Intensity (a.u.)
obs
calc
Bragg positions
obs - calc
Fit: R_p = 0.0262, R_{wp} = 0.351, χ^2 = 1.43
3T
3O
20
30
40
50
60
70
80
2θ

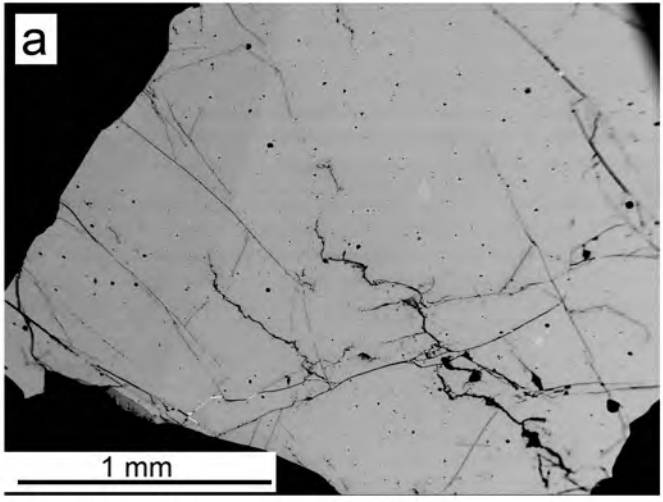

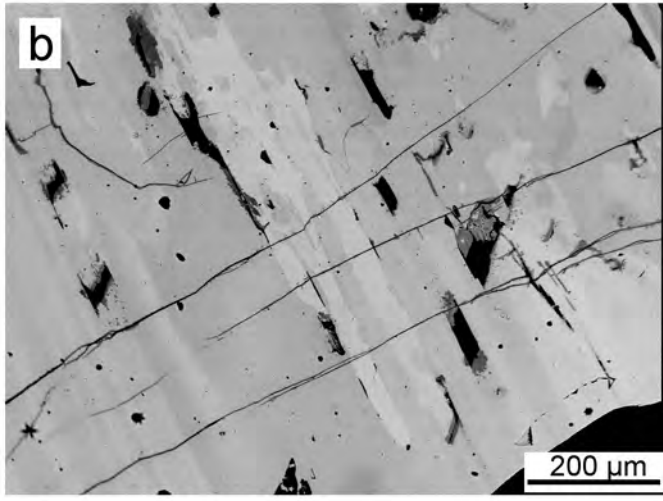

Figure 2

Figure 3

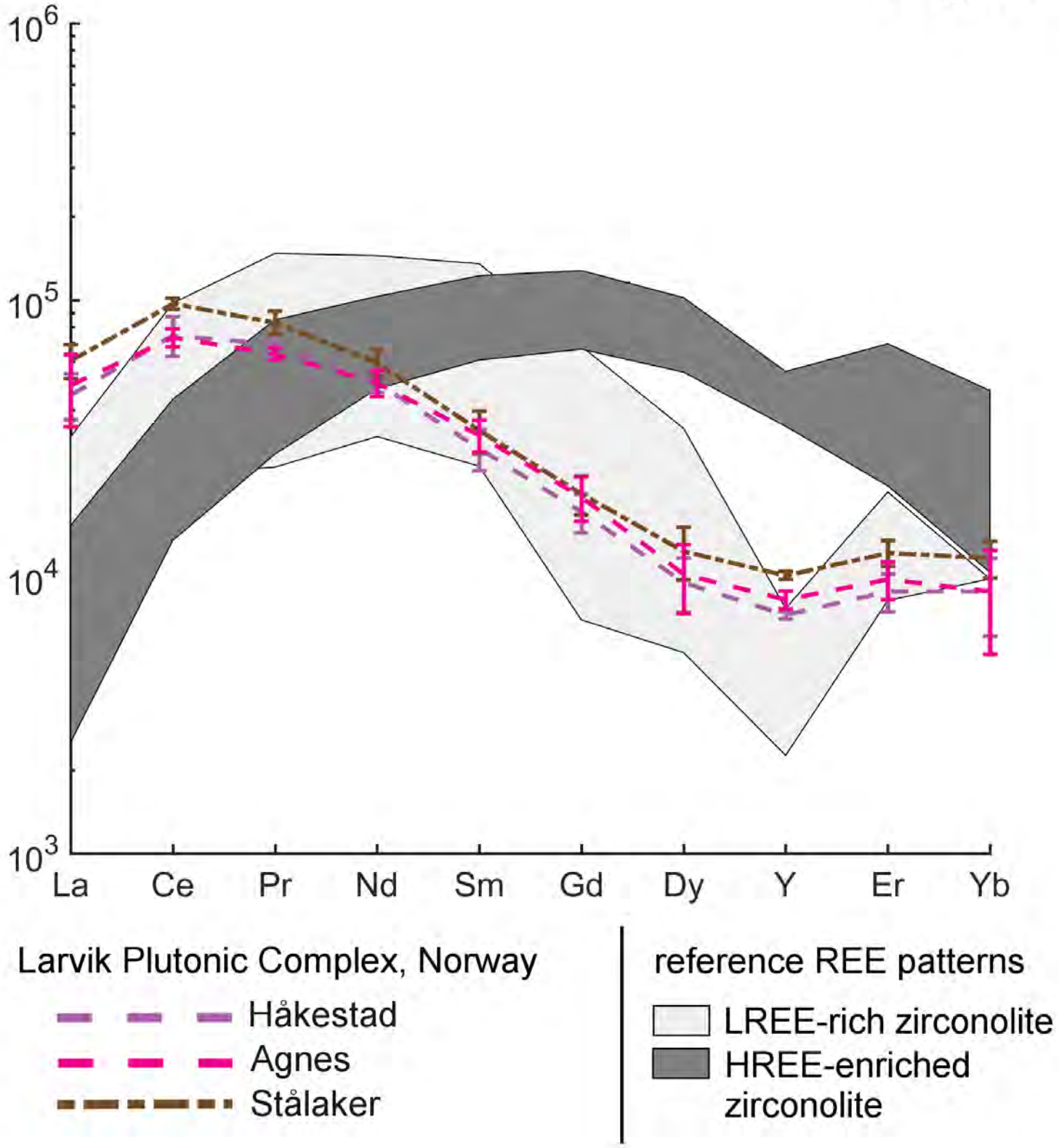
10^6
10^5
10^4
10^3
La
Ce
Pr
Nd
Sm
Gd
Dy
Y
Er
Yb
Larvik Plutonic Complex, Norway
Håkestad
Agnes
Stålaker
reference REE patterns
LREE-rich zirconolite
HREE-enriched zirconolite

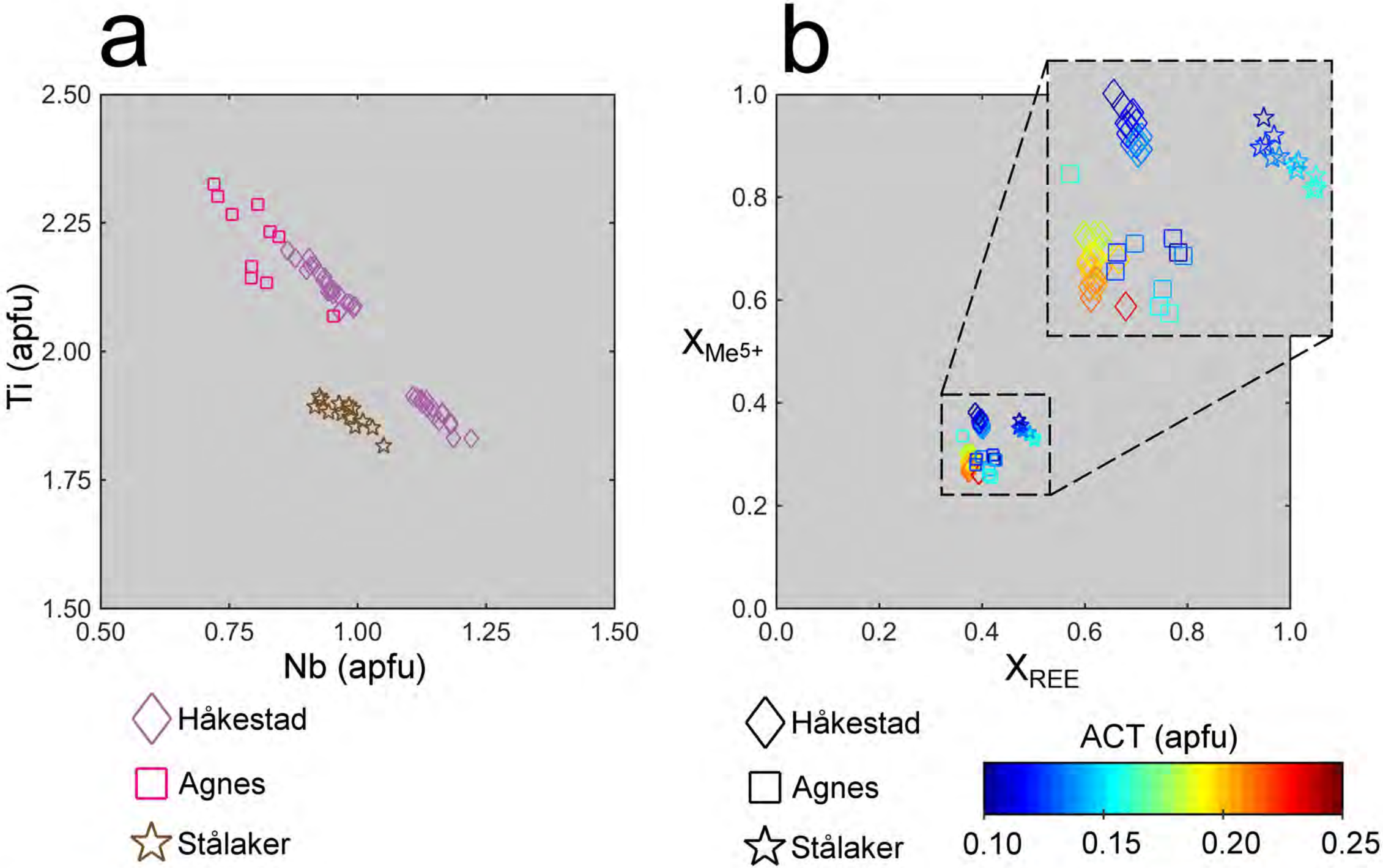
a
2.50
2.25
2.00
1.75
1.50
Ti (apfu)
0.50
0.75
1.00
1.25
1.50
Nb (apfu)
Håkestad
Agnes
Stålaker
b
1.0
0.8
0.6
0.4
0.2
0.0
$X_{Me^{5+}}$
0.0
0.2
0.4
0.6
0.8
1.0
X_{REE}
Håkestad
Agnes
Stålaker
ACT (apfu)
0.10
0.15
0.20
0.25

Figure 4

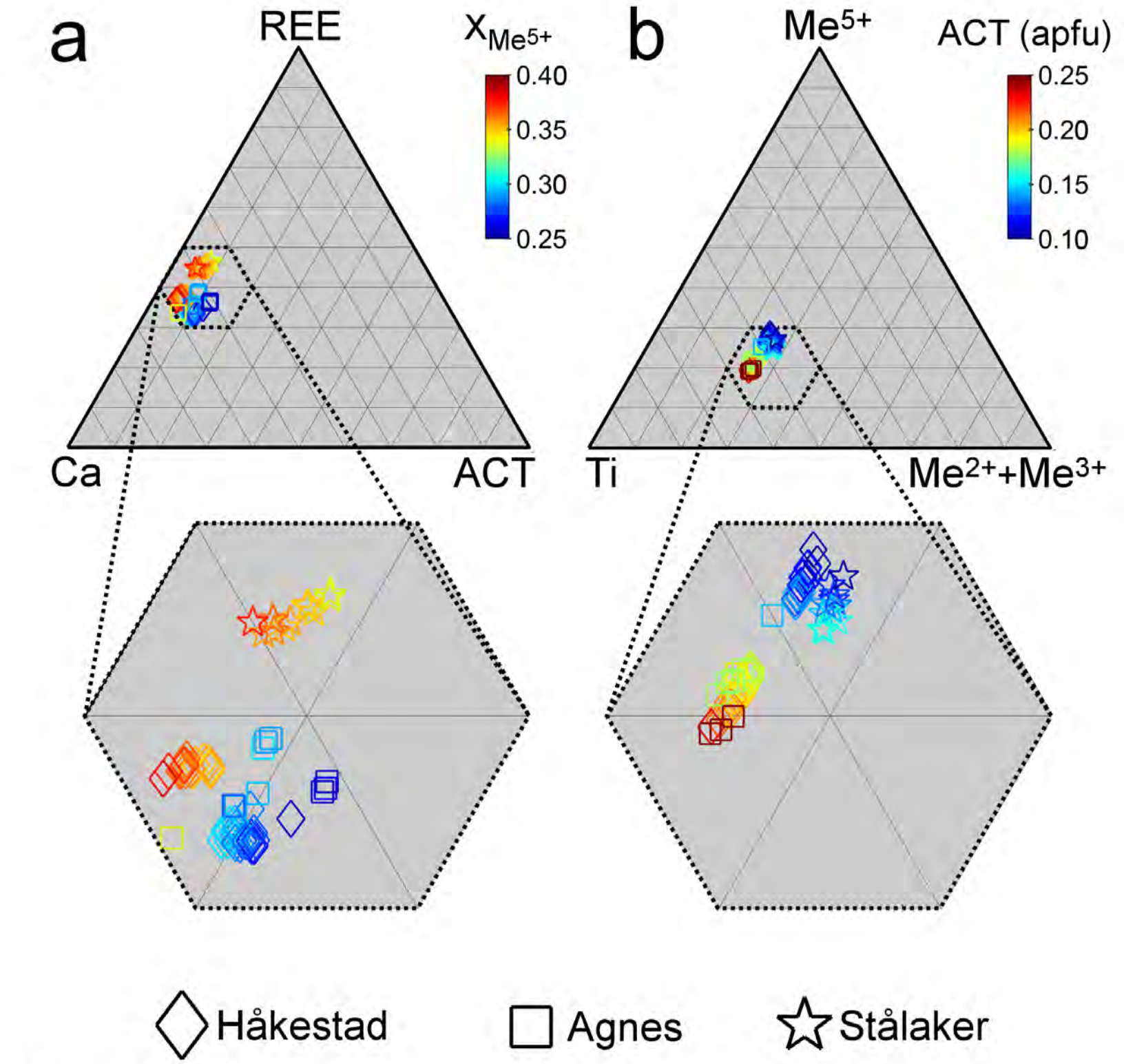
a
REE
$x_{Me^{5+}}$
0.40
0.35
0.30
0.25
Ca
ACT
b
Me^{5+}
ACT (apfu)
0.25
0.20
0.15
0.10
Ti
$Me^{2+}+Me^{3+}$
Håkestad
Agnes
Stålaker

Figure 5

Figure 6

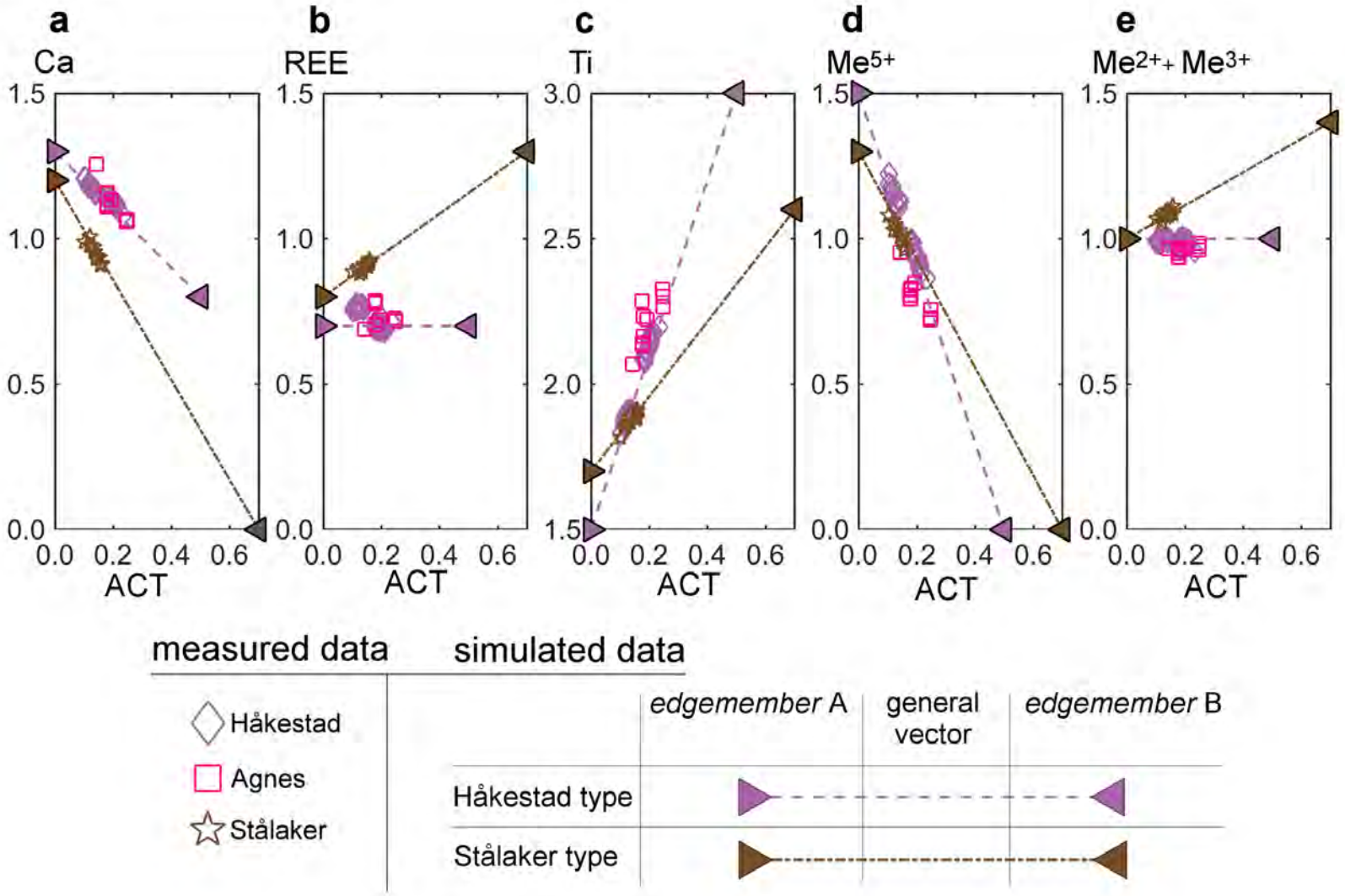
a
Ca
b
REE
c
Ti
d
Me5+
e
Me2+ + Me3+
ACT
measured data
Håkestad
Agnes
Stålaker
simulated data
edgemember A
general vector
edgemember B
Håkestad type
Stålaker type

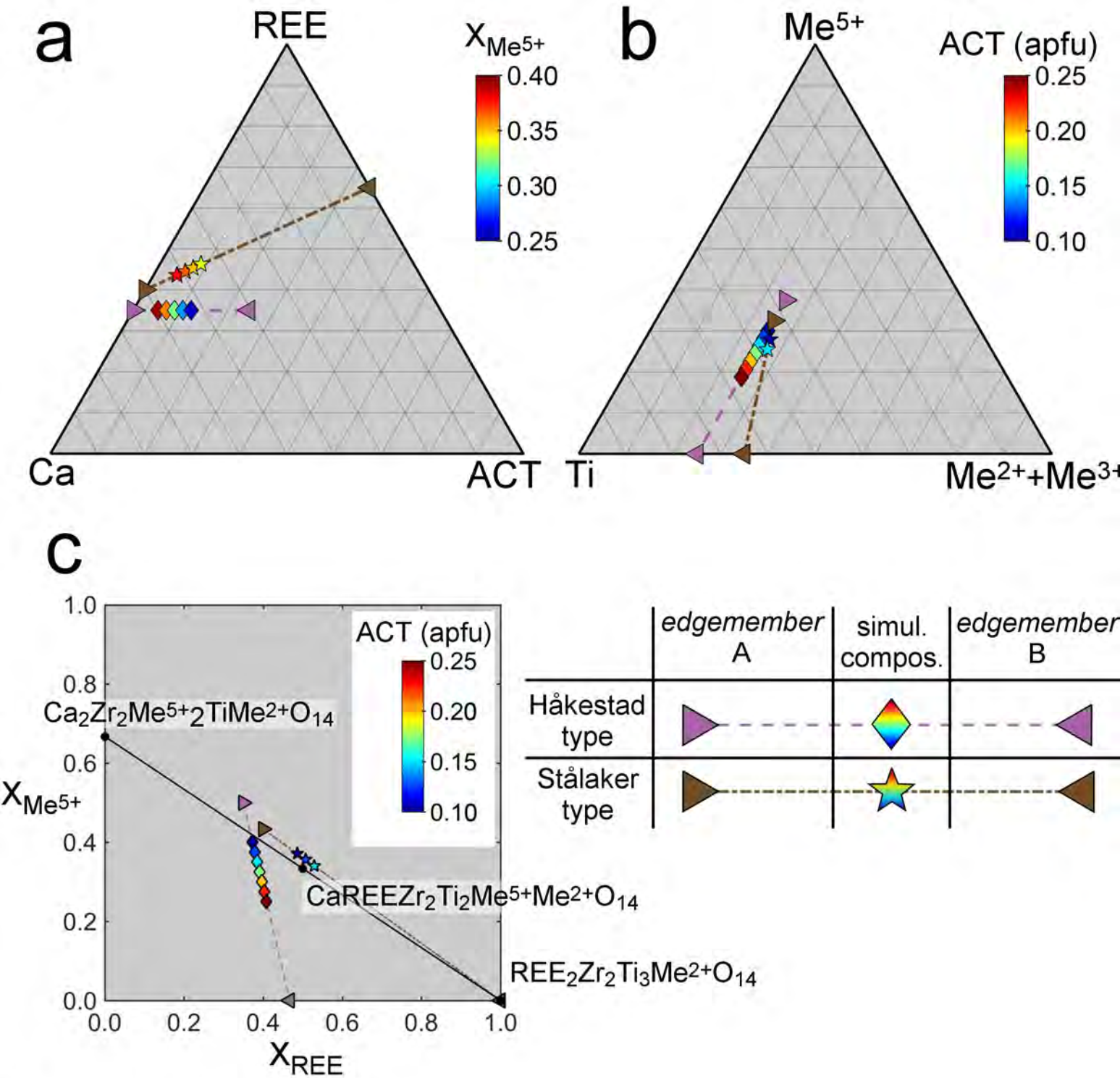
a
REE
$X_{Me^{5+}}$
0.40
0.35
0.30
0.25
Ca
ACT
b
Me^{5+}
ACT (apfu)
0.25
0.20
0.15
0.10
Ti
$Me^{2+}+Me^{3+}$
c
ACT (apfu)
0.25
0.20
0.15
0.10
$Ca_2Zr_2Me^{5+}{}_2TiMe^{2+}O_{14}$
$CaREEZr_2Ti_2Me^{5+}Me^{2+}O_{14}$
$REE_2Zr_2Ti_3Me^{2+}O_{14}$
$X_{Me^{5+}}$
X_{REE}
0.0
0.2
0.4
0.6
0.8
1.0
edgemember A
simul. compos.
edgemember B
Håkestad type
Stålaker type

Figure 7

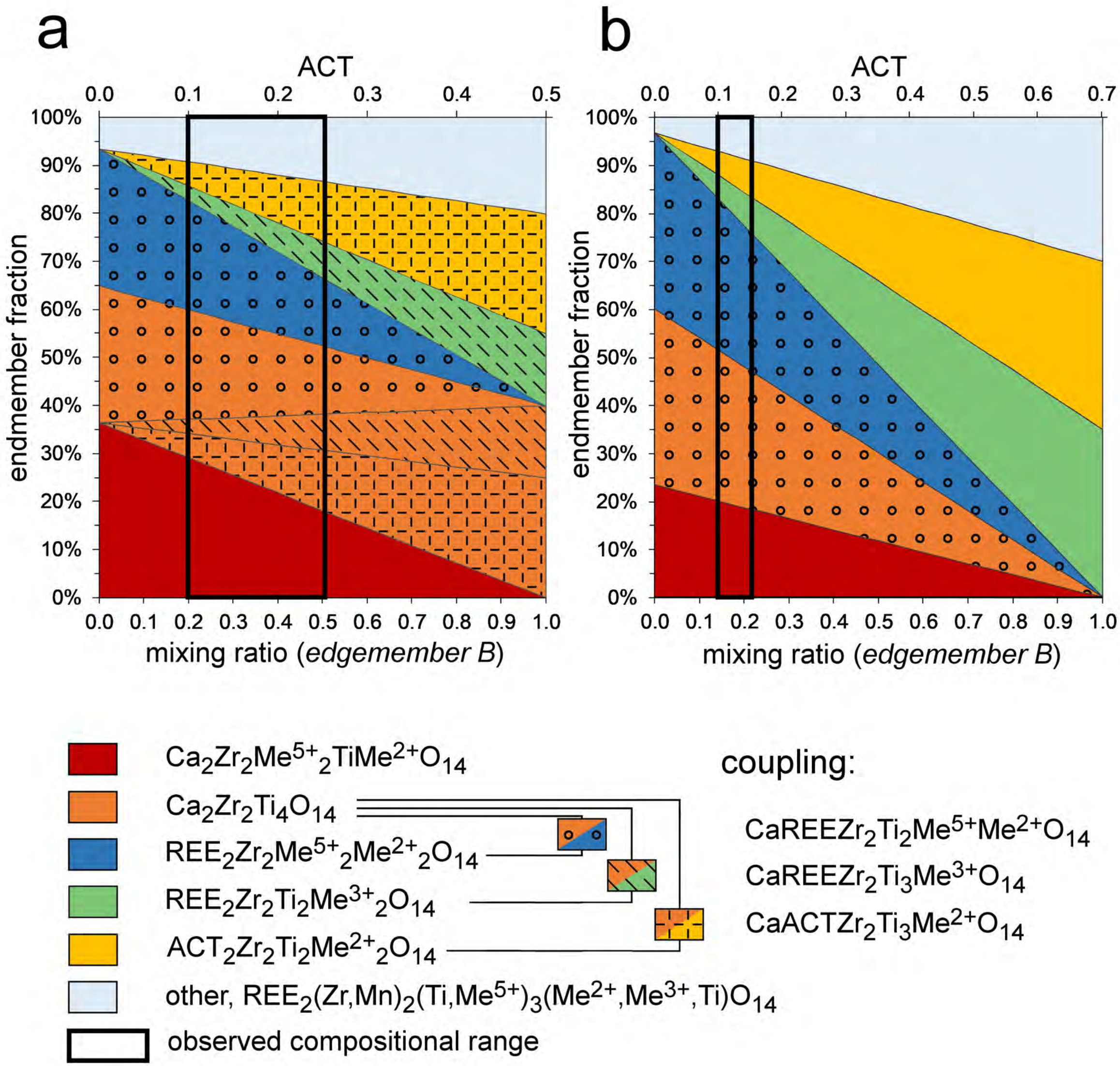
a
b
ACT
0.0 0.1 0.2 0.3 0.4 0.5
0.0 0.1 0.2 0.3 0.4 0.5 0.6 0.7
100% 90% 80% 70% 60% 50% 40% 30% 20% 10% 0%
endmember fraction
0.0 0.1 0.2 0.3 0.4 0.5 0.6 0.7 0.8 0.9 1.0
mixing ratio (*edgemember B*)
$Ca_2Zr_2Me^{5+}{}_2TiMe^{2+}O_{14}$
$Ca_2Zr_2Ti_4O_{14}$
$REE_2Zr_2Me^{5+}{}_2Me^{2+}{}_2O_{14}$
$REE_2Zr_2Ti_2Me^{3+}{}_2O_{14}$
$ACT_2Zr_2Ti_2Me^{2+}{}_2O_{14}$
other, $REE_2(Zr,Mn)_2(Ti,Me^{5+})_3(Me^{2+},Me^{3+},Ti)O_{14}$
observed compositional range
coupling:
$CaREEZr_2Ti_2Me^{5+}Me^{2+}O_{14}$
$CaREEZr_2Ti_3Me^{3+}O_{14}$
$CaACTZr_2Ti_3Me^{2+}O_{14}$

Figure 8

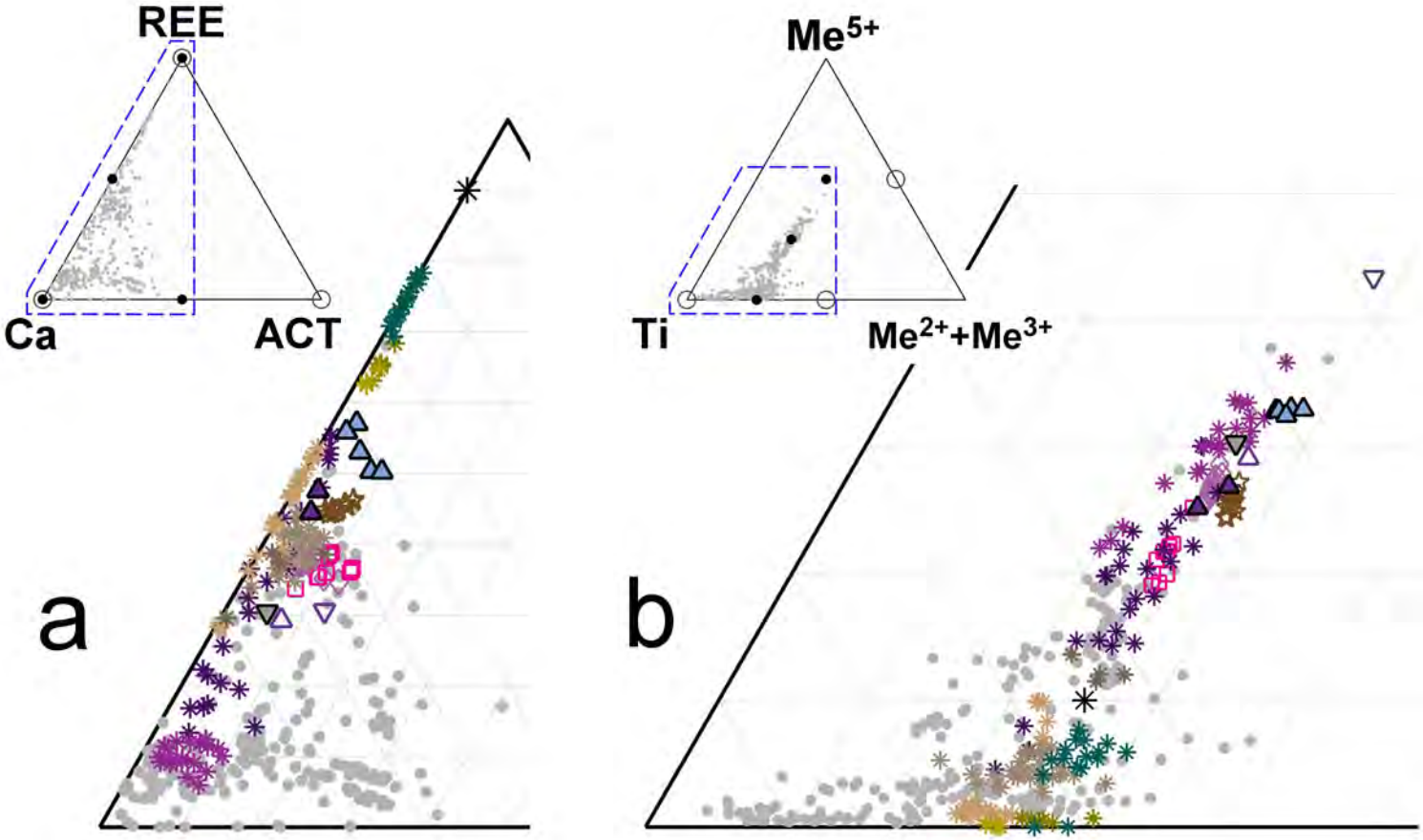

Larvik Plutonic Complex, Norway (this study)

Håkestad Agnes Stålaker

Laacher See, Germany

laachite

steffanweissite

nöggerathite

Della Ventura et al. (2000)

zirconolite-*3T* (Zubkova et al. 2018)

Dmitrovka, Ukraine

REE-rich lunar zirconolite

Schryburt Lake, Canada

Kovdor, Kola, Russia

Chilwa Island, Malawi

Koberg, Sweden

Tchivira, Angola

Vestfold Hills, Antarctica

Evate, Mozambique

other compositions worldwide

Figure 9

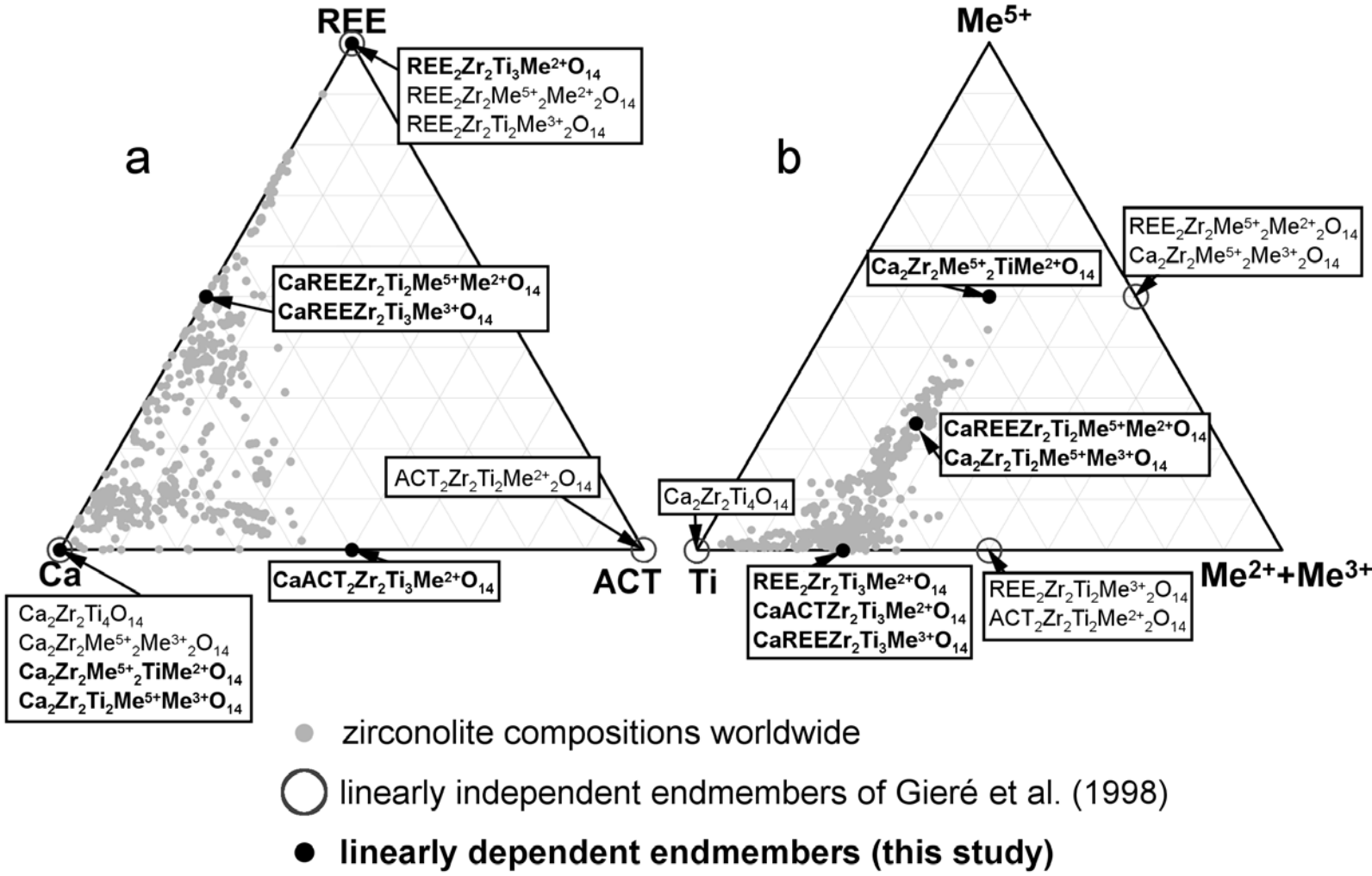
REE
a
$REE_2Zr_2Ti_3Me^{2+}O_{14}$
$REE_2Zr_2Me^{5+}{}_2Me^{2+}{}_2O_{14}$
$REE_2Zr_2Ti_2Me^{3+}{}_2O_{14}$
$CaREEZr_2Ti_2Me^{5+}Me^{2+}O_{14}$
$CaREEZr_2Ti_3Me^{3+}O_{14}$
$ACT_2Zr_2Ti_2Me^{2+}{}_2O_{14}$
Ca
ACT
$CaACT_2Zr_2Ti_3Me^{2+}O_{14}$
$Ca_2Zr_2Ti_4O_{14}$
$Ca_2Zr_2Me^{5+}{}_2Me^{3+}{}_2O_{14}$
$Ca_2Zr_2Me^{5+}{}_2TiMe^{2+}O_{14}$
$Ca_2Zr_2Ti_2Me^{5+}Me^{3+}O_{14}$
Me^{5+}
b
$REE_2Zr_2Me^{5+}{}_2Me^{2+}{}_2O_{14}$
$Ca_2Zr_2Me^{5+}{}_2Me^{3+}{}_2O_{14}$
$Ca_2Zr_2Me^{5+}{}_2TiMe^{2+}O_{14}$
$CaREEZr_2Ti_2Me^{5+}Me^{2+}O_{14}$
$Ca_2Zr_2Ti_2Me^{5+}Me^{3+}O_{14}$
$Ca_2Zr_2Ti_4O_{14}$
Ti
$REE_2Zr_2Ti_3Me^{2+}O_{14}$
$CaACTZr_2Ti_3Me^{2+}O_{14}$
$CaREEZr_2Ti_3Me^{3+}O_{14}$
$REE_2Zr_2Ti_2Me^{3+}{}_2O_{14}$
$ACT_2Zr_2Ti_2Me^{2+}{}_2O_{14}$
$Me^{2+}+Me^{3+}$
zirconolite compositions worldwide
linearly independent endmembers of Gieré et al. (1998)
linearly dependent endmembers (this study)

Figure 10

Figure 11

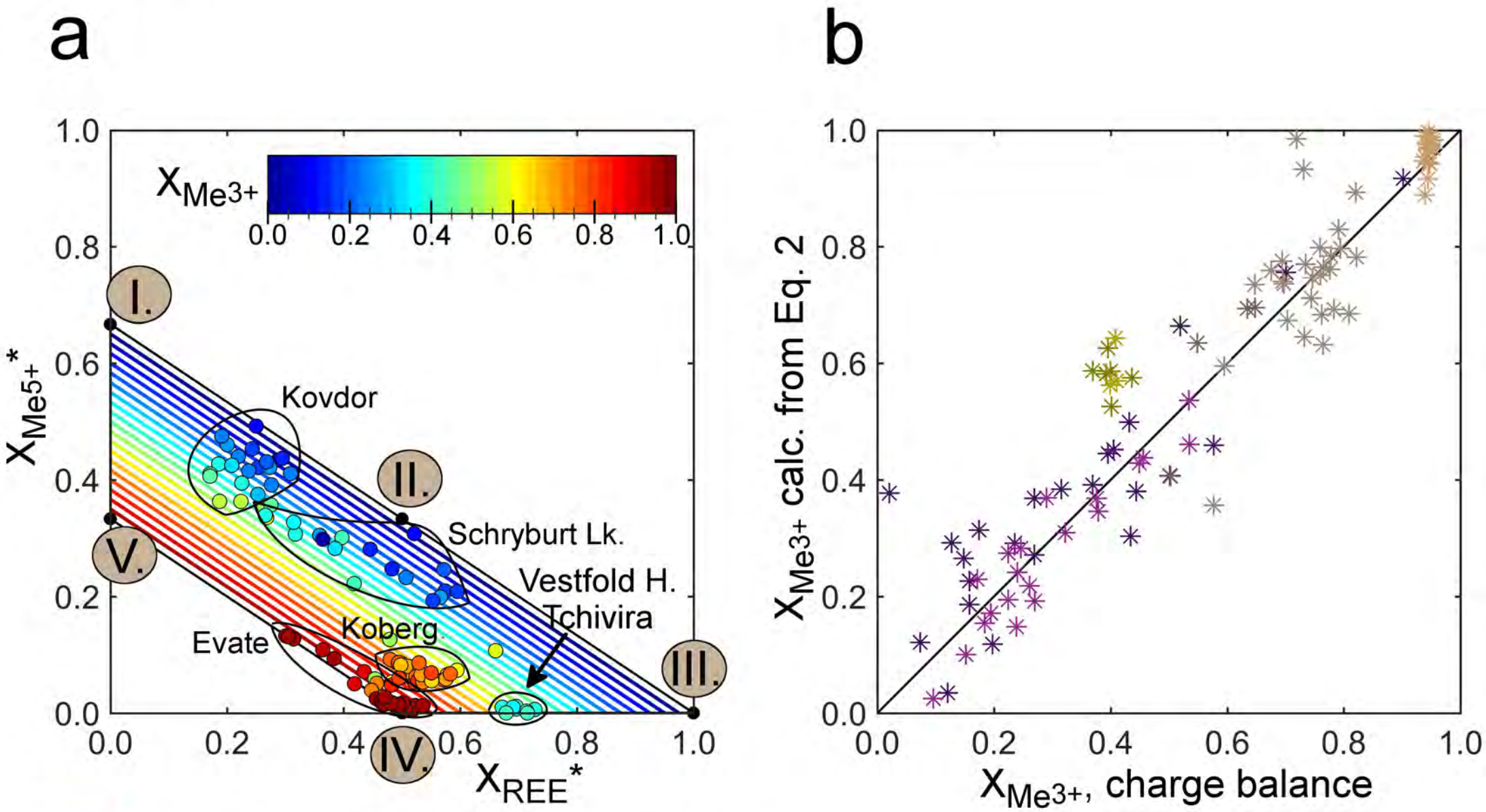

X_{Me3+} isopleths calc. from X_{REE}* and X_{Me5+}*

X_{Me3+} based on charge balance

linearly dependent endmembers:

I. $Ca_2Zr_2Me^{5+}{}_2TiMe^{2+}O_{14}$

II. $CaREEZr_2Ti_2Me^{5+}Me^{2+}O_{14}$

III. $REE_2Zr_2Ti_3Me^{2+}O_{14}$, *$CaACTZr_2Ti_3Me^{2+}O_{14}$

IV. $CaREEZr_2Ti_3Me^{3+}O_{14}$

V. $Ca_2Zr_2Ti_2Me^{5+}Me^{3+}O_{14}$

Schryburt Lake, Canada

Kovdor, Kola, Russia

Chilwa Island, Malawi

Koberg, Sweden

Tchivira, Angola

Vestfold Hills, Antarctica

Evate, Mozambique

perfect agreement (1:1)